ARTICLE IN PRESS

Nature Communications

https://doi.org/10.1038/s41467-026-71644-0

Article in Press

Heterointerface-engineered ZnO/CuO bimetallic sites enable pollutant-directed conversion with in situ catalyst regeneration

Received: 18 December 2025

Accepted: 25 March 2026

Cite this article as: Zhang, Z.-Q., Xu, X.-W., Duan, P.-J. *et al.* Heterointerface-engineered ZnO/CuO bimetallic sites enable pollutant-directed conversion with in situ catalyst regeneration. *Nat Commun* (2026). https://doi.org/10.1038/s41467-026-71644-0

Zhi-Quan Zhang, Xiao-Wei Xu, Pi-Jun Duan, Ying Shao, Que Wang, Zhi-Hao Qin, Chang-Wei Bai, Xin-Jia Chen, Jing Wang, Fu-Qiao Yang & Fei Chen

We are providing an unedited version of this manuscript to give early access to its findings. Before final publication, the manuscript will undergo further editing. Please note there may be errors present which affect the content, and all legal disclaimers apply.

If this paper is publishing under a Transparent Peer Review model then Peer Review reports will publish with the final article.

ARTICLE IN PRESS

© The Author(s) 2026. **Open Access** This article is licensed under a Creative Commons Attribution-NonCommercial-NoDerivatives 4.0 International License, which permits any non-commercial use, sharing, distribution and reproduction in any medium or format, as long as you give appropriate credit to the original author(s) and the source, provide a link to the Creative Commons licence, and indicate if you modified the licensed material. You do not have permission under this licence to share adapted material derived from this article or parts of it. The images or other third party material in this article are included in the article's Creative Commons licence, unless indicated otherwise in a credit line to the material. If material is not included in the article's Creative Commons licence and your intended use is not permitted by statutory regulation or exceeds the permitted use, you will need to obtain permission directly from the copyright holder. To view a copy of this licence, visit http://creativecommons.org/licenses/by-nc-nd/4.0/.

Heterointerface-Engineered ZnO/CuO Bimetallic Sites Enable Pollutant-Directed Conversion with In Situ Catalyst Regeneration

Zhi-Quan Zhang[1, #], Xiao-Wei Xu[1, #], Pi-Jun Duan[1, #], Ying Shao[1, #], Que-Wang[1], Zhi-Hao Qin[1], Chang-Wei Bai[1], Xin-Jia Chen[1], Jing Wang[1], Fu-Qiao Yang[1], Fei Chen[1, **]

[1]Key Laboratory of the Three Gorges Reservoir Region's Eco-Environment, Ministry of Education, College of Environment and Ecology, Chongqing University, Chongqing 400045, China

[#]They contributed equally to this work

[**]**Corresponding Authors**：

Prof. Fei Chen, E-mail: fchen0505@cqu.edu.cn

Abstract

Polymerization-based wastewater treatment offers reduced oxidant demand and product recovery, yet practical application is hindered by catalyst fouling and unselective reactions due to single-site competition. Here, we report a readily synthesized and scalable ZnO/CuO catalyst featuring dual functional sites that decouple pollutant and oxidant activation. Zn sites preferentially adsorb/activate organics, whereas Cu sites predominantly activate the oxidant. This site differentiation programs two pathway regimes governed by pollutant electronic structure: electron-transfer-mediated polymerization for electron-rich substrates and radical-induced mineralization for electron-deficient substrates. Importantly, radicals generated during mineralization depolymerize the accumulated foulant layer in situ, effecting autonomous catalyst regeneration with a 2.5-fold performance recovery and reduced external regeneration demand. Process performance is validated in a 200 L self-circulating reactor, maintaining 98% removal efficiency for both pollutant classes over ten cycles. Toxicological profiling across multiple biological models, supported by metabolomics, confirmed effective detoxification of multi-pollutant wastewater, including restoration of normal metabolic function in zebrafish (e.g., lipid and glutathione metabolism). This study establishes a dual-site cooperative catalysis framework that leverages intrinsic wastewater chemistry for self-regeneration, showcasing a complete trajectory from atomic-scale design to reactor-scale implementation.

Introduction

Polymerization-based advanced oxidation processes (P-AOPs) offer a low-carbon route for concurrent pollutant abatement and resource recovery, owing to high reaction selectivity, reduced oxidant demand, and the prospect of value-added product reclamation [1, 2]. However, translation to real wastewater remains constrained by several factors. First, large disparities in molecular size, charge, and hydrophobicity between pollutants and oxidants hinder their synergistic activation at a single catalytic site, limiting both efficiency and pathway control [3, 4]. Second, electron-rich pollutants preferentially undergo polymerization, and the resulting polymeric deposits accumulate on the catalyst surfaces, blocking active sites and inducing deactivation [5, 6]. High-temperature calcination affords only partial regeneration at substantial energy cost. Third, polymerization is intrinsically selective for electron-rich pollutants and exhibits poor removal of electron-deficient compounds prevalent in complex effluents [7]. Thus, P-AOPs face three persistent challenges in wastewater treatment: inefficient dual-substrate activation, fouling-induced catalyst deactivation, and narrow pollutant applicability.

Traditional mineralization-based heterogeneous AOPs (M-AOPs) address the selectivity gap by employing catalyst-activated oxidants to generate highly reactive species, notably hydroxyl radicals ($^{\bullet}OH$) and sulfate radicals ($SO_4^{\bullet-}$), enabling non-selective degradation and mineralization of diverse organics [8]. Yet, radical-dominated pathways are vulnerable to quenching by inorganic ions and dissolved organic matter [9]. Moreover, these systems typically require high oxidant dosages and convert pollutants predominantly to CO_2, outcomes that run counter to carbon-neutrality objectives and preclude resource recovery. These complementary strengths and weaknesses motivate an integrated strategy that couples polymerization with mineralization, harnessing the advantages of each while mitigating their respective limitations.

Catalyst design is central to realizing such integration. Prevailing approaches emphasize single-substrate (oxidant) activation using single-site architectures, often neglecting pollutant activation and the construction of dedicated sites[10, 11, 12]. Inevitably, pollutants and oxidants competitively adsorb at the same sites, depressing turnover and confounding pathway selectivity (Fig. 1). Emerging evidence suggests that reaction routing is governed by a cooperative catalyst–pollutant system, not the catalyst alone [13, 14]. Consequently, bifunctional, dual-site catalysts (one site tailored to pollutants and the other to oxidants) could spatially decouple activation events, enabling programmable switching between polymerization and mineralization according to pollutant electronic structure.

For practical deployment in wastewater treatment, dual-site catalysts should feature simple synthesis, scalable manufacture, operational stability, and ecological safety. Zinc oxide (ZnO) is attractive on these grounds [15]; the relatively low electronegativity of Zn facilitates electronic interaction with organics, favoring adsorption/activation of pollutants. In contrast, copper sites in copper oxide (CuO) possess higher electronegativity and strong oxygen affinity, promoting selective adsorption and activation of oxidants [16, 17]. Rational integration of ZnO and CuO thus provides complementary active sites for spatially separated activation of pollutants (Zn) and oxidants (Cu). Moreover, the Fermi-level mismatch across the ZnO/CuO heterointerface establishes a built-in electric field (BIEF) that drives directional electron transfer and modulates interfacial charge dynamics [18]. Such an architecture furnishes a mechanistic basis to implement pollutant-directed polymerization and controlled radical mineralization within one catalyst, creating a pathway to address dual-substrate activation, fouling resistance via in situ depolymerization, and broad pollutant coverage.

Guided by the above analysis, ZnO and CuO were selected as the basis for a dual-site catalyst, and a facile hydrothermal–calcination route was developed to obtain bifunctional ZnO/CuO. In this unique design, Zn sites preferentially adsorbed and activated pollutants, whereas Cu sites selectively activated the oxidant. This site differentiation enabled dynamic pathway selection according to pollutant electronic structure: electron-rich substrates underwent electron-transfer-mediated polymerization, while electron-deficient substrates followed radical-induced mineralization. A key feature of the system was autonomous regeneration: radicals formed during mineralization depolymerized the accumulated foulant layer in situ, and the regenerated catalyst exhibited a 2.5-fold performance enhancement. Thus, the dual-site design simultaneously mitigated deactivation and provided continuous self-renewal under operating conditions. Theoretical calculations elucidated the site-specific adsorption energetics and clarified how pollutant electronics bias pathway selection, rationalizing the observed switching behavior. To assess practicality, a 200 L self-circulating reactor was constructed, demonstrating stable operation and effective treatment at scale. Comprehensive toxicological assessment using multiple biological models and metabolomics confirmed effective water purification and detoxification. Overall, this study defines a dual-site catalytic platform that couples pollutant-directed selectivity with in situ catalyst regeneration, offering actionable design principles for practical wastewater remediation.

Results

Rational Synthesis and Structural Characterization of the Bimetallic-Site Catalysts

A facile hydrothermal-calcination route yielded a bifunctional ZnO/CuO catalyst with gram-scale productivity (Fig. 2a) [19]. X-ray diffraction (XRD) confirmed phase-pure ZnO and CuO, with reflections indexed to ZnO (PDF #36-1451) and CuO (PDF #45-0937), evidencing successful composite formation (Fig. 2b) [20, 21]. Fourier-transform infrared (FTIR) spectroscopy probed interfacial bonding (Fig. 2c): bands at 465 cm^{-1} (Zn-O) and 536 cm^{-1} (Cu-O) shifted to 500 cm^{-1} upon hybridization, indicating the formation of Zn-O/Cu-O structures and the integration of the two oxides [22, 23]. Transmission electron microscopy (TEM) showed spherical ZnO particles intimately interfaced with dense CuO nanoclusters (Fig. 2d, Supplementary Figs. 2-4). High-resolution TEM identified lattice spacings of 0.245 nm and 0.253 nm, corresponding to the (101) plane of ZnO and the (002) plane of CuO, respectively (Figs. 2e-f, Supplementary Figs. 5-6) [24, 25]. These observations established an intimately coupled ZnO/CuO heterointerface with potential for synergistic catalysis.

To resolve oxidation states and coordination environments, we combined X-ray photoelectron spectroscopy (XPS) with X-ray absorption fine structure (XAFS) analyses (Supplementary Figs. 7-16). High-resolution XPS spectra showed Zn 2*p* core-level peaks at 1022.0 eV ($2p_{3/2}$) and 1045.1 eV ($2p_{1/2}$), consistent with Zn^{2+} (Fig. 2g) [26]. Similarly, the Cu 2*p* region exhibited characteristic peaks at 933.7 eV ($2p_{3/2}$) and 953.6 eV ($2p_{1/2}$), confirming the presence of Cu^{2+} (Fig. 2h) [27]. Importantly, positive shifts of Zn 2*p* and negative shifts of Cu 2*p* relative to the pristine oxides indicate electron transfer from ZnO to CuO, evidencing strong electronic coupling at the heterointerface [28]. These charge-transfer signatures motivated a deeper analysis of local structure by X-ray Absorption Fine Structure (XAFS).

The valence states and local coordination of Zn and Cu atoms were further probed by X-ray absorption near-edge structure (XANES) and extended X-ray absorption fine structure (EXAFS). The Zn *K*-edge XANES spectrum (Fig. 2i) of the ZnO/CuO composite closely matched the reference ZnO, indicating that Zn primarily existed in the +2 oxidation state [29]. Similarly, the Cu *K*-edge spectrum exhibited an absorption profile nearly identical to that of CuO, confirming Cu^{2+} as the dominant state (Fig. 2j) [17]. These findings were consistent with the XPS results. Fourier-transform EXAFS (FT-EXAFS, phase-uncorrected R-space) (Fig. 2k) for Zn showed two prominent peaks at ~1.46 Å and ~2.98 Å, attributable to Zn-O and Zn-Zn scattering paths of ZnO within the composite [30]. Notably, both peaks exhibited slight shifts compared to pure ZnO, indicating a perturbed Zn coordination sphere due to CuO incorporation and supporting the presence of a strongly coupled ZnO/CuO heterointerface [31]. Similarly, the Cu *K*-edge FT-EXAFS spectrum (Fig. 2l) displayed peaks at ~1.47 Å and ~2.49 Å, attributed to Cu-O and Cu-Cu paths of CuO in the composite [32]. Their observable shifts compared with pure CuO further corroborate substantial interfacial interactions in the ZnO/CuO composite [33]. Critically, no Zn-Zn (Zn foil) and Cu-Cu (Cu foil) contributions are detected, excluding metallic clustering and implying high dispersion of both cations within the heterostructure [34, 35]. Wavelet transform (WT)-EXAFS (Figs. 2m-n) further resolved overlapping backscattering contributions and clearly discriminates Zn-O, Cu-O, Zn-Zn, and Cu-Cu signals. In sum, these results provided direct evidence of strong interfacial interactions at the ZnO/CuO heterointerface and confirmed enhanced electronic coupling between the two oxide phases.

Catalytic Activity and Matrix Robustness of the Fenton-Like Reaction System

To assess the efficacy of the dual-site ZnO/CuO catalyst for oxidant activation toward pollutants of contrasting electronic character, we employed bisphenol A (BPA; electron-rich) and atrazine (ATZ;

electron-deficient) as model substrates, using peroxymonosulfate (PMS) as the oxidant. Optimal concentrations of ZnO/CuO, PMS, BPA, and ATZ were established a priori (Supplementary Figs. 17-22). Unless otherwise specified, all experiments were conducted under consistent conditions. Control tests showed negligible adsorption of BPA or ATZ on ZnO, CuO, or ZnO/CuO (Fig. 3a, Supplementary Fig. 23). Neither PMS alone nor homogeneous Cu^{2+}-activated PMS effected appreciable removal (Supplementary Figs. 23-25). By contrast, the ZnO/CuO catalyst exhibited efficient PMS activation, achieving complete removal of BPA and ATZ within 5 min (Fig. 3a-d). Pseudo-first-order rate constants in the ZnO/CuO/PMS system were 13.0 and 5.8 times higher than those in the physically mixed ZnO+CuO/PMS control. (Fig. 3b, e, Supplementary Figs. 26-27), evidencing a synergistic heterostructure effect beyond simple mixture.

To compare oxidant utilization across substrate regimes, PMS consumption was quantified. Within 5 min, 74% of PMS was consumed for BPA versus 55% for ATZ (Supplementary Fig. 28), suggesting distinct activation pathways and degradation kinetics. Consistent with this trend, total organic carbon (TOC) analysis showed rapid BPA mineralization (87.7% at 6 min), far exceeding that of ATZ (35.4%) (Supplementary Fig. 29). Matrix-tolerance tests further differentiated the systems. The BPA regime maintained stable performance in the presence of common inorganic ions and across varied water matrices (Supplementary Figs. 30-32). The ATZ regime also showed robust anti-interference behavior, but high chloride ion (Cl^-) partially inhibited removal, consistent with radical quenching in a radical-dominated pathway (Supplementary Figs. 33-35). Both systems showed high tolerance to dissolved organic matter (DOM), with minimal loss in the presence of humic acid or bovine hemoglobin, indicating suitability for complex waters (Fig. 3f, Supplementary Figs. 36-39). The ZnO/CuO/PMS system remained effective over pH 3.0-9.0 (Fig. 3g, Supplementary Figs. 40-41) and displayed a broad substrate scope, achieving near-complete removal within 5 min for phenol (PhOH), 4-chlorophenol (4-CP), ortho-chlorophenol (OCP), 2,4-dimethylphenol (2,4-DMP), sulfamethoxazole (SMX), sulfadiazine (SDZ), and sulfapyridine (SPY) (Fig. 3h). These results demonstrated the efficient water purification and strong practical potential of the ZnO/CuO/PMS system.

Despite comparable single-cycle performance, cycling tests revealed divergent stability (Supplementary Fig. 42). The BPA removal progressively declined with repeated runs, whereas ATZ removal remained stable. We attributed this contrast to pathway-dependent surface evolution: electron-rich BPA underwent electron-transfer-mediated polymerization, leading to polymeric deposit accumulation and active-site blockage (Figs. 3i-j). Electron-deficient ATZ followed a radical-dominated mineralization route that did not generate polymeric foulants, preserving activity. Based on these observations, we hypothesized that, in mixed-pollutant matrices, in situ-generated strong oxidizing radicals could depolymerize the accumulated foulant layer, enabling catalyst self-regeneration. The following experiments were designed to test this hypothesis.

Multi-Probe Recognition of Reactive Species and Catalytic Pathways

To resolve the dominant oxidizing pathways in the ZnO/CuO/PMS/BPA and ZnO/CuO/PMS/ATZ, we implemented a comprehensive quenching protocol. The scavengers used were: tert-butanol (TBA) for hydroxyl radicals ($^{\bullet}OH$), methanol (MeOH) for sulfate radicals ($SO_4^{\bullet-}$), TEMPOL and p-benzoquinone (p-BQ) for superoxide radicals ($^{\bullet}O_2^{-}$), *L*-histidine and *β*-carotene for singlet oxygen ($^1O_2$), dimethyl sulfoxide (DMSO) and methyl phenyl sulfoxide (PMSO) for high-valent metal species, and potassium dichromate ($K_2Cr_2O_7$) for electrons. In the BPA system, various quenchers produced minor or negligible inhibition of pollutant decay (Fig. 4a). Even when radical scavenger concentrations were increased from 20 mM to 200 mM, both removal efficiency and apparent rate constant remained essentially unchanged (Fig. 4b, Supplementary Figs. 44-45), suggesting that neither radical species (e.g., $^{\bullet}OH$, $SO_4^{\bullet-}$, $^{\bullet}O_2^{-}$) nor non-radical species (e.g., $^1O_2$ or high-valent copper) governed the reaction. By contrast, adding an electron scavenger led to a substantial suppression of BPA degradation (Supplementary Fig. 46), implicating a catalyst-mediated electron-transfer pathway (ETP) as the primary mechanism. In the ATZ system, MeOH markedly inhibited degradation: increasing MeOH from 0 to 100 mM reduced the removal from 99.2% to 27.3% and the rate constant from 0.92 to 0.07

min^{-1}, indicating that $SO_4^{\bullet-}$ served as the primary role species (Fig. 4c, Supplementary Figs. 47-48). Probe experiments corroborated this finding (Supplementary Fig. 49), while quenching results showed limited contributions from $^1O_2$ and high-valent metal species (Supplementary Fig. 50). Given the electron-deficient nature of ATZ, non-radical electrophilic routes are disfavored. The quenching data initially indicated ETP-dominant BPA oxidation and radical-dominated ATZ degradation. Electron spin resonance provided direct spectroscopic support. In the ZnO/CuO/PMS/BPA system, no detectable signals for $^{\bullet}OH$, $SO_4^{\bullet-}$, or $^1O_2$ were detected, consistent with a non-radical, electron-transfer-driven process. (Fig. 4d). In contrast, the ZnO/CuO/PMS/ATZ system exhibited a strong $SO_4^{\bullet-}$ signal, confirming that $SO_4^{\bullet-}$ were the predominant active species (Fig. 4e).

To further elucidate the intrinsic catalytic activity and electron transfer pathways of ZnO/CuO, a series of electrochemical experiments was conducted. Open-circuit potential measurements showed an immediate increase upon PMS dosing at the ZnO/CuO electrode (Fig. 4f), indicating an activated surface complex (ZnO/CuO-PMS*) with enhanced oxidizing capacity [36]. Subsequent addition of BPA induced a sharp potential drop, consistent with electron donation from BPA to ZnO/CuO-PMS* complex and thus catalyst-mediated ETP [37]. Chronoamperometry (*i-t*, Fig. 4f) [38] further substantiated this assignment: sequential additions of PMS and then BPA produced stepwise current increases, evidencing electron flow from BPA (donor) to PMS (acceptor) facilitated by ZnO/CuO [39]. Salt-bridge experiments yielded distinct current responses upon separate addition of PMS and BPA (Supplementary Fig. 51), reinforcing the through-catalyst electron-shuttle scenario. In contrast, ATZ additions caused negligible changes in OCP and current, excluding a significant ETP contribution and aligning with a radical-mediated mechanism. Electrochemical impedance spectroscopy (EIS) showed lower charge-transfer resistance for ZnO/CuO than for ZnO, CuO, or the physical mixture ZnO+CuO (Fig. 4g, Supplementary Fig. 53), confirming that heterojunction formation enhanced interfacial electron transport [40]. Resistance decreased sharply upon PMS addition, consistent with ZnO/CuO-PMS* complex formation, and decreased further after BPA dosing, supporting accelerated electron transfer in the BPA regime (Supplementary Figs. 54-55) [41]. No appreciable change was observed upon

ATZ addition (Supplementary Fig. 56), again consistent with a radical-dominated ATZ pathway. Linear sweep voltammetry (LSV) corroborated these trends: ZnO/CuO showed substantially higher current density than ZnO, CuO, or their physical mixture (Fig. 4h), increased immediately after PMS dosing (active complex formation), and rose further upon BPA addition (pollutant-promoted electron transfer) [10 42]. In the ATZ system, LSV showed no appreciable current increase after ATZ addition, in agreement with radical-driven oxidation without enhanced electron shuttling.

Dual-Function Catalysis at Zn-Cu Biphasic Sites via Interfacial Electron Coupling

To clarify how dual-site synergy governs the distinct degradation regimes, we deconvoluted the roles of Zn and Cu. In situ Raman of ZnO/CuO system upon PMS dosing displayed a distinct peak at 834 cm^{-1}, attributed to the PMS^* surface complex (Fig. 5a) [43]. Control tests with ZnO and CuO showed that this PMS^* feature appeared only on CuO (Figs. 5b-c), indicating that Cu sites preferentially adsorbed/activated PMS. PMS utilization corroborated this assignment: ZnO consumed 1.0% PMS, versus 39.7% for CuO and 73.6% for ZnO/CuO (Supplementary Fig. 57). Moreover, Cu-site masking nearly abolished degradation (Supplementary Fig. 58). Although ZnO alone scarcely activated PMS, its integration with CuO substantially boosted PMS utilization, consistent with a BIEF within the heterojunction that accelerated interfacial electron transfer and, in turn, PMS activation. After establishing the Cu role, we examined Zn. XPS after reaction revealed pronounced carbon accumulation on ZnO, whereas CuO showed negligible changes (Supplementary Fig. 59), indicating that Zn sites preferentially interacted with organics, while Cu sites activated PMS, constituting a dual-functional division of labor.

Density Functional Theory (DFT) further supported this interpretation (Atomic coordinates for the structural model are available in Supplementary Data 1). Calculations showed more exergonic PMS adsorption on Cu site than on Zn site (-1.92 eV *vs.*-0.91 eV) (Fig. 5d). Elongation of the O-O bond in PMS was also more pronounced on Cu sites (1.477 Å *vs.* 1.469 Å), consistent with stronger PMS activation at Cu, in agreement with in situ Raman, PMS utilization, and masking results. For pollutants, Zn sites in ZnO/CuO display enhanced adsorption of BPA and ATZ, with adsorption energies strengthened by 1.55 eV and 0.84 eV, respectively, relative to pristine ZnO (Fig. 5e), while Cu sites show weaker adsorption (Fig. 5f). Thus, Zn preferentially adsorbed/engaged pollutants, consistent with XPS. Furthermore, *d*-band center analysis further differentiated functions: the Zn site exhibited a downshift in the heterostructure relative to pristine ZnO (-4.70 eV *vs.* -5.13 eV), suggesting reduced PMS affinity (Fig. 5g). Whereas the *d*-band center of the Cu site remained essentially unchanged (-2.01 eV *vs.* -2.04 eV), supporting its primary role in PMS activation. The experimental-computational evidence established a well-defined division of functions: Zn sites adsorbed/activated organic substrates, and Cu sites activated PMS, with synergy mediated by interfacial electron coupling.

To elucidate the interfacial electron coupling mechanism between ZnO and CuO, work function analysis was performed. ZnO exhibited a lower work function (Φ = 5.70 eV) compared to CuO (Φ = 8.51 eV), indicating a greater tendency to act as an electron donor (Fig. 5h). Upon contact, electrons flowed from ZnO to CuO until Fermi-level equilibration, establishing a BIEF (ZnO→CuO). Bader charge analysis quantified this interfacial charge redistribution, revealing an electron transfer of 1.15 e^- from ZnO to CuO (Fig. 5i). This field and charge redistribution, together with pollutant electronics, dictate pathway selection. For electron-rich substrates, pollutants acted as auxiliary electron donors, augmenting ZnO→CuO electron flux under the BIEF. The resulting electron-rich interface promoted PMS reduction to SO_4^{2-} and sustained electron-transfer pathways (ETP). For electron-deficient substrates, electron donation was disfavored; limited electron availability biases PMS toward O–O cleavage and formation of $SO_4^{\bullet-}$/ $^{\bullet}OH$, i.e., a radical-dominated route. This framework rationalized the ETP-dominant behavior of BPA versus the radical-dominant behavior of ATZ.

DFT with molecular orbital (MO) analysis of the ZnO/CuO–PMS complex and a set of ten representative pollutants (Fig. 5j) elucidated the electronic prerequisite for ETP [13]. In the ZnO/CuO/PMS system, ETP required electron donation from the highest occupied molecular orbital (HOMO) of pollutants to the lowest unoccupied molecular orbital (LUMO) of the ZnO/CuO-PMS complex [37]. Therefore, a smaller energy gap between the complex's LUMO and the pollutant's HOMO was thermodynamically favored by ETP. High-lying HOMO substrates (e.g., BPA and SMX) exhibited small ΔE and thus preferentially underwent ETP rather than radical oxidation. In contrast, electron-deficient pollutants (e.g., ATZ, BA) possessed lower HOMO energies, yielding larger ΔE and higher barriers for electron transfer; radical oxidation therefore prevailed. These results explained the divergent mechanisms in BPA vs ATZ systems and demonstrated that Fenton-like efficiency and pathway in ZnO/CuO/PMS were co-governed by catalyst electronic structure and pollutant frontier orbitals, validating the "zone-specific activation and cooperative reaction" design.

In Situ Depolymerization Enables Self-regenerating Catalysts with Practical Performance

To verify that radical-driven mineralization can remove polymeric foulants in situ, we examined mixed-substrate systems. When BPA and ATZ coexisted, polymerization preferentially consumed BPA prior to mineralization (Fig. 6a), consistent with literature indicating a lower activation barrier and thermodynamic favorability for polymerization over mineralization [44]. This sequence established conditions under which radicals produced during mineralization could subsequently depolymerize the accumulated polymers. Thermogravimetric analysis (TGA) showed a larger weight loss for the catalyst after the BPA-only reaction than for the pristine material (Fig. 6b), evidencing polymer deposition. Following ATZ/PMS treatment, the weight-loss fraction decreased, indicating removal of surface-bound polymers (Fig. 6b). Elemental analysis corroborated this trend: C and O contents increased after BPA exposure and declined after ATZ/PMS treatment (Fig. 6c). Functionally, a catalyst subjected to ten cycles with high BPA concentration exhibited attenuated PMS activation and stagnant BPA removal, consistent with active-site blockage. By contrast, a catalyst subsequently treated with ATZ/PMS displayed a 2.5-fold performance recovery (Fig. 6d). TEM further confirmed substantial reduction or removal of surface polymers after mineralization treatment (Fig. 6f) [45]. Together, these results demonstrate effective in situ depolymerization of polymeric foulants and catalyst regeneration via the mineralization pathway. In BPA-only cycling, removal efficiency declined over successive runs, whereas introducing ATZ maintained stable, high BPA removal (Fig. 6e). These observations indicate that radicals generated during ATZ activation mediate in situ decomposition of BPA-derived polymers, thereby sustaining long-term activity and stability of the catalytic system.

To evaluate the practical potential of this synergistic system, a pilot-scale study was conducted using a 200 L self-circulating reactor operating without external mixing (Fig. 6g). The reactor exploited hydraulic head differences and an internal slope to achieve spontaneous circulation (Fig. 6h, Supplementary Fig. 78). The catalyst was immobilized on polyurethane sponges (32 units in series) suspended in the wastewater, which enhanced contact among catalyst, oxidant, and pollutants, facilitated recovery/reuse, and minimized secondary contamination [46]. In mixed-wastewater operation, the system sustained 98% (BPA) and 96% (ATZ) removal over ten consecutive cycles (Fig. 6i), demonstrating operational robustness at pilot scale.

To quantify environmental performance, we conducted a life cycle assessment (LCA) of the ZnO/CuO/PMS process against ZnO/PMS and CuO/PMS comparators (Supplementary Figs. 79-82), covering catalyst synthesis through pollutant degradation and evaluating 18 impact categories. The dual-site ZnO/CuO/PMS system exhibited lower impact scores across all categories relative to single-component benchmarks, indicating superior environmental compatibility (Supplementary Fig. 83) [47]. Notably, the 200 L pilot displayed ~10 orders of magnitude lower aggregate impact scores than laboratory-scale setups (Supplementary Fig. 84), reflecting substantial gains in eco-efficiency. Overall, the ZnO/CuO/PMS platform, coupled with cost-effectiveness, environmental compatibility, and operational sustainability, supporting its scalability as a practical water purification technology.

Matrix-Robust Detoxification and Safety Profiling of Catalytic Processes

The ecological safety and practical relevance of the ZnO/CuO/PMS system were assessed across microbial, plant, and animal models to capture toxicity outcomes for both the polymerization and mineralization pathways. Two representative bacterial strains, Gram-negative Escherichia coli (*E. coli*) and Gram-positive Staphylococcus aureus (*S. aureus*), were selected as microbial toxicity models

(Supplementary Fig. 85). Colony-forming assays showed that solutions containing untreated BPA or ATZ strongly inhibited growth of both strains, evidencing high baseline toxicity. In contrast, post-treatment solutions from the ZnO/CuO/PMS process restored bacterial growth to control levels, indicating effective detoxification under both pathways.

For plant-based toxicity assessment, Chlorella vulgaris and wheat seedlings served as model systems. Wheat exposed to treated solutions exhibited stem lengths comparable to controls (Supplementary Figs. 86-87), whereas untreated pollutant solutions significantly suppressed growth. Consistently, Chlorella cultures in treated solutions showed higher optical density (OD) and chlorophyll a content than in untreated matrices (Supplementary Fig. 88), confirming substantial reduction of phytotoxicity by either pathway.

Multi-parameter assays in zebrafish were further conducted to evaluate organism-level safety [48, 49]. Zebrafish exposed to treated solutions showed no morphological abnormalities, cardiac dysfunction, or mortality during 96 h, matching control outcomes (Figs. 7a-b). This contrasted sharply with the developmental deformities, cardiac abnormalities, and mortality in the untreated groups. Body length in treated cohorts did not differ significantly from controls, indicating normal growth (Figs. 7c-f). Fluorescent imaging of intracellular reactive oxygen species (ROS) revealed weak signals in control and treated groups, whereas intense fluorescence in untreated BPA exposure indicated substantial ROS accumulation and oxidative stress (Figs. 7g-i) [50, 51].

To probe systemic effects of BPA and the extent of detoxification, untargeted metabolomics was performed in zebrafish [52, 53]. Relative to controls, BPA exposure yielded 720 significantly altered metabolites (345 up-regulated, 325 down-regulated; Fig. 7j), predominantly in lipids and lipid-like molecules, organheterocycles, and nucleotides (Fig. 7k). Kyoto Encyclopedia of Genes and Genomes (KEGG) enrichment analysis indicated perturbations in lipid metabolism, pyrimidine metabolism, purine metabolism, glutathione metabolism, alanine metabolism, and ABC transporters (Fig. 7l). These pathway disruptions align with oxidative stress, developmental dysregulation, and energy imbalance; notably, dysregulated nucleotide and lipid metabolism can directly impair embryonic development [54, [55, 56]. Furthermore, disturbed glutathione metabolism weakened antioxidant defenses, thus promoting ROS accumulation and oxidative stress-induced damage in zebrafish [57, 58]. These molecular signatures were concordant with the observed developmental defects and ROS stress in untreated BPA groups and demonstrated that the ZnO/CuO/PMS treatment restored metabolic homeostasis and suppressed oxidative injury.

Across bacteria, algae, plants, and zebrafish, the ZnO/CuO/PMS system mitigated toxicity to near-control levels and reversed pollutant-induced metabolic disturbances, particularly in pathways integral to development and antioxidant defense. These findings established the platform's dual function, an efficient water purification technology coupled with robust protection of aquatic health, and supported its suitability for safe and practical deployment.

Discussion

This study reported an easily synthesized, scalable ZnO/CuO dual-site catalyst that enabled simultaneous activation of oxidants and pollutants. The structural design decouples functions: Zn sites preferentially adsorb/activate pollutants, whereas Cu sites selectively activate the oxidant. This site differentiation supported dynamic pathway selection governed by pollutant electronics: electron-rich contaminants underwent electron-transfer-mediated polymerization, whereas electron-deficient compounds followed radical-induced mineralization. Furthermore, radicals formed during mineralization depolymerized polymeric deposits in situ, effecting autonomous catalyst regeneration with a 2.5-fold performance enhancement. By utilizing intrinsic wastewater constituents, this self-restoration strategy reduced energy consumption and operational costs. Process viability was validated in a 200 L self-circulating reactor, sustaining 98% and 96% removal for the two pollutant classes over ten cycles. Toxicological profiling across multiple biological models, supported by metabolomics, confirmed effective detoxification of multi-pollutant wastewater, including restoration of zebrafish physiological functions (e.g., lipid and glutathione metabolism). This work establishes a dual-site cooperative catalysis framework, overcomes the limitation of inefficient co-activation at single sites, elucidates a self-regenerative mechanism for in situ catalyst renewal, and provides actionable design principles for practical wastewater treatment.

Methods

Chemicals and reagents. Detailed information is provided in the Supplementary Information.

Characterizations. The crystalline structures of the synthesized materials were characterized by X-ray diffraction (XRD; Rigaku Ultima IV, Japan) using Cu Kα radiation over a 2θ range of 10°-80°. Transmission electron microscopy was performed using a JEOL JEM-F200 instrument operated at an accelerating voltage of 200 kV and equipped with a JEOL EX-37270VUP energy-dispersive X-ray spectrometer for elemental analysis. Chemical states were analyzed using X-ray photoelectron spectroscopy (XPS; ESCALAB Xi$^+$, Thermo Fisher Scientific, USA) with a monochromatic Al Kα source (12.5 kV). Fourier-transform infrared (FT-IR) spectra were acquired on a Thermo Scientific iN10 spectrometer with KBr as background reference. Electron spin resonance (ESR) measurements were conducted on a Bruker ER200-SRC spectrometer using 5,5-dimethyl-1-pyrroline N-oxide (DMPO) and 2,2,6,6-tetramethyl-4-piperidone (TEMP) as spin-trapping agents. Electrochemical properties were evaluated with a CHI660E electrochemical workstation (Chenhua, China) configured with a standard three-electrode system comprising a catalyst-modified glassy carbon working electrode, platinum wire counter electrode, and Ag/AgCl (saturated KCl) reference electrode. Total organic carbon (TOC) content was quantified using a CD800s analyzer (Hangzhou Qikun Technology Co., China). XANES spectra at the Zn and Cu K-edges were collected in transmission mode on a laboratory-scale XAFS instrument (easyXAFS300, easyXAFS LLC). The spectrometer used Rowland circle geometry with spherically bent crystal analyzers and an Ag X-ray tube source, and detection was performed with a silicon drift detector (AXAS-M1, KETEK GmbH).

Catalytic performance evaluation. Degradation experiments were performed in 50 mL aqueous suspensions containing the synthesized catalyst (0.1 g L^{-1}) and either PMS 0.3 mM + BPA 10 mg L^{-1} or PMS 0.5 mM + ATZ 10 mg L^{-1}. Prior to oxidant dosing, the catalyst was pre-equilibrated with the respective pollutant by stirring for 5 min to establish adsorption–desorption equilibrium. After PMS addition, 1 mL aliquots were withdrawn at 1-min intervals and immediately quenched with 0.1 mL of 100 mM sodium thiosulfate to terminate the reaction. Samples were then centrifuged at 18630 g for 20 min to remove suspended particles, and the resulting supernatants were analyzed for BPA or ATZ by high-performance liquid chromatography (HPLC; Agilent 1260 Infinity, Agilent Inc., USA).

Density functional theory (DFT) calculations. All DFT calculations were performed within the generalized gradient approximation (GGA) using the Perdew-Burke-Ernzerhof (PBE) exchange-correlation functional. The Brillouin zone was sampled with a 1*1*1 k-points mesh for geometry optimization. A plane-wave basis set with a kinetic energy cutoff of 400 eV was employed to describe valence electrons, and a Gaussian smearing width of 0.05 eV was applied for partial orbital occupation. Electronic and geometric convergence criteria were set to 10^{-5} eV and 0.02 eV $Å^{-1}$, respectively. A vacuum layer of 20 Å was introduced along the non-periodic direction to suppress spurious interactions between periodic images. Van der Waals interactions were accounted for using the Grimme DFT+D3 empirical correction scheme.

Catalyst preparation. (a) Preparation of ZnO/CuO: First, 2 mmol $Zn(NO_3)_2$•$5H_2O$, 2 mmol $Cu(NO_3)_2$•$3H_2O$, and 4 mmol citric acid were dissolved in 45 mL of ethanol and stirred for 30 min. Subsequently, the solution underwent solvothermal reaction at 120 °C for 20 h. After washing with ethanol and drying, the intermediate product was calcined at 350°C for 2 h with a heating rate of 2°C min^{-1}, yielding the final ZnO/CuO material.

(b) Preparation of ZnO: ZnO was synthesized using a procedure identical to that of ZnO/CuO, except for the omission of $Cu(NO_3)_2$•$3H_2O$.

(c) Preparation of CuO: CuO was synthesized using a procedure identical to that of ZnO/CuO, except for the omission of $Zn(NO_3)_2$•$5H_2O$.

Determination of pollutant concentrations and their degradation intermediates. The concentration of target pollutants was determined using a high-performance liquid chromatograph (1260 Infinity, Agilent Technologies, USA) equipped with a ZORBAX SBC-18 column (5 μm, 4.6 × 250 mm), maintained at a column temperature of 35 ± 1°C, and fitted with a UV detector. For BPA detection, the mobile phase consisted of acetonitrile and 0.2% acetic acid aqueous solution (60:40 v/v), with a flow rate of 1.0 mL min^{-1} and an injection volume of 20 μL. The detection wavelength was set at 273 nm, and the analysis time was 6 min. For SMX detection, the mobile phase consisted of acetonitrile and 0.1% formic acid aqueous solution (40:60 v/v), with a flow rate of 1.0 mL min^{-1} and an injection volume of 20 μL. The detection wavelength was set at 269 nm, and the analysis time was 6 min. For ATZ detection, the mobile phase consisted of acetonitrile and 0.2% acetic acid aqueous solution (60: 40 v/v), with a flow rate of 1.0 mL min^{-1}, injection volume of 20 μL. The detection wavelength was set to 272 nm, and the analysis time was 6 min. Testing conditions for other pollutants are detailed in Supplementary Table 17.

BPA degradation products were characterized by liquid chromatography-mass spectrometry (LC-MS) using an Agilent 6460 HPLC system coupled to an API 3000 mass analyzer, with separation performed on a Kromasil C18 column (4.6 × 250 mm). All other analytical conditions matched those employed for BPA concentration quantification.

Pilot-scale experiments for treating 200 L of BPA wastewater and mixed wastewater. Thirty-two polyurethane sponge blocks (5 cm × 5 cm × 5 cm) were employed as catalyst supports due to their porous structure and ease of recovery. To prepare the catalyst-loaded sponges, 10 g of catalyst was dispersed in a mixture of 100 mL of ethanol and 2 mL of Nafion, followed by ultrasonication to achieve homogeneous catalyst distribution. The resulting suspension was uniformly coated onto the 32 sponge units, establishing the foundation for subsequent wastewater treatment experiments. For BPA wastewater degradation experiments, the initial BPA concentration was set at 2.5 mg L^{-1} with 0.1 mM PMS. Each treatment cycle lasted 2 hours. Upon cycle completion, the BPA concentration was restored to 2.5 mg L^{-1}, and additional PMS was introduced, with ten consecutive cycles performed to evaluate catalyst efficiency and durability. In mixed wastewater treatment, the system contained 2.5 mg L^{-1} BPA and 2.5 mg L^{-1} ATZ initially, with the PMS concentration increased to 0.2 mM while maintaining other experimental conditions identical to those described above.

Assessment of toxicity by *E. coli* and *S. aureus* culture experiments. Activated bacterial strains were prepared by inoculating 50 μL of frozen *E. coli* and *S. aureus* stock into LB medium. The culture was incubated at 37°C with shaking at 180 rpm for 10 h in a rotary incubator (Honour, HNY-200B). Subsequently, fresh LB medium was supplemented with solutions collected from various reaction systems. The activated *E. coli* and *S. aureus* culture was transferred to this conditioned medium and incubated under identical conditions for an additional 10 hours. Following incubation, the bacterial suspension was adjusted to an optical density of 0.1 at 600 nm (OD_{600} = 0.1) using sterile deionized water. Serial ten-fold dilutions were performed to achieve a final dilution factor of 10^6, and 100 μL aliquots of the diluted suspensions were spread onto agar plates. After 18 h of incubation at 37°C, bacterial growth was assessed by colony counting. All procedures were conducted in a laminar flow cabinet (AIRTECH, SW-CJ-1FD), with consumables sterilized by autoclaving at 121°C for 15 min (IMJ-85A, STIK Co., USA) or by exposure to 254 nm ultraviolet radiation for 20 min.

No statistical method was used to predetermine the sample size. No data were excluded from the analyses. The experiments were not randomized. The Investigators were not blinded to allocation during experiments and outcome assessment.

Toxicity assessment by wheat seed culture experiments. The influence of various post-treatment solutions on wheat growth was systematically investigated using a hydroponic cultivation system. Uniformly plump wheat seeds were selected and surface-sterilized by immersion in 3% hydrogen peroxide (H_2O_2) for 20 min, followed by thorough rinsing with deionized water. Twenty seeds were evenly arranged on filter paper in petri dishes and supplied with 8 mL of solution from different treatment systems. The dishes were maintained at 25°C under a 12-hour light/12-hour dark photoperiod with a light intensity of 3000 lux. Wheat growth was monitored at 24-hour intervals, and solutions were periodically replenished to maintain consistent moisture levels. Upon stabilization of germination rates, indicating completion of the primary sprouting phase, stem lengths were measured to assess seedling growth. Continuous observation throughout the experimental period enabled comprehensive evaluation of treatment effects on plant development and potential phytotoxicity.

No statistical method was used to predetermine the sample size. No data were excluded from the analyses. The experiments were not randomized. The Investigators were not blinded to allocation during experiments and outcome assessment.

Toxicity assessment by Chlorella vulgaris culture. *Chlorella vulgaris* was cultivated in BG-11 medium within conical flasks placed in an illuminated incubator under controlled conditions (25 ± 1 °C, 4000 lux illumination, 12 h/12 h light/dark cycle) for 10 days. Cells harvested during the logarithmic growth phase ($OD_{680} \approx 0.5$) were then transferred to fresh BG-11 medium prepared using water from different experimental groups, including blank controls, untreated BPA or ATZ solutions, and treated BPA or ATZ samples. All media and solutions were sterilized by autoclaving (121 °C, 20 min) prior to use. Biomass accumulation (OD_{680}) and chlorophyll a content were monitored at daily intervals across all experimental conditions.

No statistical method was used to predetermine the sample size. No data were excluded from the analyses. The experiments were not randomized. The Investigators were not blinded to allocation during experiments and outcome assessment.

Determination of chlorophyll a. Chlorophyll a concentration was determined spectrophotometrically after acetone extraction according to established protocols. Specifically, 10 mL aliquots of algal culture were centrifuged at 10000 rpm for 10 min. The resulting pellets were resuspended in 10 mL of 90% (v/v) acetone and maintained in complete darkness at 4 ℃ for 24 h to ensure thorough pigment extraction. Absorbance readings were obtained at 750, 663, 645, and 630 nm using a UV-vis spectrophotometer with 90% acetone serving as the blank reference. The concentration of chlorophyll a was calculated using the following equation:

$$\text{Chlorophyll a (mg L}^{-1}\text{)} = 11.64 \times (OD_{663} - OD_{750}) - 2.16 \times (OD_{645} - OD_{750}) + 0.1 \times (OD_{630} - OD_{750}) \qquad \text{(S1)}$$

Toxicity assessment by zebrafish culture experiments. To obtain a sufficient number of viable embryos, three healthy zebrafish (one female and two males) were housed together in nutrient-enriched water for 12 h. The collected embryos were thoroughly rinsed with water from the aquaculture system to remove potential surface contaminants. Under microscopic examination, embryos at the eight-cell developmental stage were specifically selected and separated for subsequent experimental procedures. Exposure solutions were prepared for different experimental groups: the treatment group received solutions collected from various reaction systems; the blank control group was maintained in nutrient solution alone; and the pollutant control group was exposed to untreated BPA or ATZ solutions. The embryos were distributed into 24-well plates, with each well containing 1 mL of nutrient solution and 1 mL of the designated exposure solution, and one embryo per well (n=10 per group). From the initiation of exposure until zebrafish hatching, embryonic development was monitored every 24 h using microscopy. These observations aimed to assess the teratogenic effects of the exposure solutions on both embryonic and larval stages, ensuring accurate and reliable evaluation of potential developmental toxicity. Intracellular reactive oxygen species (ROS) in zebrafish larvae were detected using the fluorescent probe DCFH-DA. After 120 hours of exposure, larvae were incubated with 10 μM DCFH-DA in darkness at 28 °C for one hour. ROS levels were subsequently visualized and analyzed using an AE31E inverted fluorescence microscope.

All zebrafish experiments were conducted in accordance with the guidelines of the China Laboratory Animal Administration and approved by the Laboratory Animal Welfare and Ethics Committee of the Third Military Medical University, under license No. SCXK (Yu) 20170002. No statistical method was used to predetermine the sample size. No data were excluded from the analyses. The experiments were not randomized. The Investigators were not blinded to allocation during experiments and outcome assessment.

References

1. Zhang, Y. J., et al. Simultaneous nanocatalytic surface activation of pollutants and oxidants for highly efficient water decontamination. *Nat. Commun.* **13**, 3005 (2022).
2. Liu, H. Z., et al. Tailoring d-band center of high-valent metal-oxo species for pollutant removal via complete polymerization. *Nat. Commun.* **15**, 2327 (2024).
3. Shi, L.-J., et al. Dual-substrate synergistic catalysis for highly efficient water purification. *Nat. Water* **3**, 345-353 (2025).
4. Shi, L. J., et al. Anions-Impacted Water Purification from a Dual-Substrate Perspective. *Environ. Sci. Technol.* **59**, 12378-12386 (2025).
5. Rui, J., et al. Revolutionizing water treatment: Polymerization pathways in advanced oxidation processes. *Appl. Catal. B-Environ. Energy* **380**, 125747 (2026).
6. Duan, P. J., et al. Polymeric products deactivate carbon-based catalysts in catalytic oxidation reactions. *Nat. Water* **3**, 178-190 (2025).
7. Zhao, X. & Zhang, Z. Heterogeneous Peroxymonosulfate-Based Advanced Oxidation Mechanisms: New Wine in Old Bottles? *Environ. Sci. Technol.* **59**, 5913-5924 (2025).
8. Lee, J., von Gunten, U. & Kim, J. H. Persulfate-Based Advanced Oxidation: Critical Assessment of Opportunities and Roadblocks. *Environ. Sci. Technol.* **54**, 3064-3081 (2020).
9. Yang, X., Rosario-Ortiz, F. L., Lei, Y., Pan, Y., Lei, X. & Westerhoff, P. Multiple Roles of Dissolved Organic Matter in Advanced Oxidation Processes. *Environ. Sci. Technol.* **56**, 11111-11131 (2022).
10. Pei, J., et al. Non-metallic iodine single-atom catalysts with optimized electronic structures for efficient Fenton-like reactions. *Nat. Commun.* **16**, 800 (2025).
11. Liu, C., Li, J., He, X., Yue, J., Chen, M. & Chen, J. P. The "4 + 1" strategy fabrication of iron single-atom catalysts with selective high-valent iron-oxo species generation. *Proc. Natl. Acad. Sci. USA.* **121**, 2322283121 (2024).
12. Zhu, Z.-S., et al. Multidimensional engineering of single-atom cobalt catalysts for ultrafast Fenton-like reactions. *Nat. Water* **3**, 211-221 (2025).

13. Guo, J., et al. Fenton-like activity and pathway modulation via single-atom sites and pollutants comediates the electron transfer process. *Proc. Natl. Acad. Sci. USA.* **121**, e2313387121 (2024).
14. Yang, M., et al. Unveiling the Origins of Selective Oxidation in Single-Atom Catalysis via Co-N_4-C Intensified Radical and Nonradical Pathways. *Environ. Sci. Technol.* **56**, 11635-11645 (2022).
15. Zhang, Z. Q., et al. Nano-island-encapsulated cobalt single-atom catalysts for breaking activity-stability trade-off in Fenton-like reactions. *Nat. Commun.* **16**, 115 (2025).
16. Zhou, X., et al. Identification of Fenton-like active Cu sites by heteroatom modulation of electronic density. *Proc. Natl. Acad. Sci. USA.* **119**, 2119492119 (2022).
17. Lin, J., et al. In-Situ Formed Zr-Phosphonate Surface Complex Promotes Peroxymonosulfate Activation of Single-Atom Cu for Efficient Phosphonate Oxidation. *Environ. Sci. Technol.* **59**, 15547-15557 (2025).
18. Chen, C., et al. Built-In Electric Field Augments Hypersalinity Resistance of Heterostructured Metal Oxides for Efficient Fenton-like Catalysis. *ACS Nano* **19**, 29616-29626 (2025).
19. Liu, L., et al. Coordination Reconstruction Enhanced Synergistic Nonradical Oxidation Pathways in Cobalt Single-Atom Catalysts for Sustained Pollutant Destruction. *Angew. Chem. Int. Ed.* **64,** e202508330 (2025).
20. Luo, L., et al. Binary Au-Cu Reaction Sites Decorated ZnO for Selective Methane Oxidation to C1 Oxygenates with Nearly 100% Selectivity at Room Temperature. *J. Am. Chem. Soc.* **144**, 740-750 (2022).
21. Liu, Z., et al. Co_3O_4/CuO@C catalyst based on cobalt-doped HKUST-1 as an efficient peroxymonosulfate activator for pendimethalin degradation: Catalysis and mechanism. *J. Hazard. Mater.* **478**, 135437 (2024).
22. Hao, S., et al. Photocatalytic Coupling of CH_4 and CO_2 to Ethanol on Asymmetric Ce−O−Zn Sites. *Adv. Funct. Mater.* **34**, 2314118 (2023).
23. Li, J., et al. Engineering ZnO/CuO Heterojunctions via Supramolecular Mediation Leading to

Morphology-Dependent High-Performance Piezoelectric Catalyst. *Small*, e07661 (2025).

24. Pang, J., et al. Tailoring Dual High-Valence Cu-O-Mn Active Sites to Enhance VOC Catalytic Oxidation. *Environ. Sci. Technol.* **59**, 9812-9826 (2025).
25. Zhang, Z. Q., Duan, P. J., Bai, C. W., Chen, X. J., Wang, J. & Chen, F. Surface-hydroxylated single-atom catalyst with an isolated Co-O-Zn configuration achieves high selectivity in regulating active species. *Nat. Commun.* **16**, 2376 (2025).
26. Zhang, Y., et al. Single-Atom Sn on Tensile-Strained ZnO Nanosheets for Highly Efficient Conversion of CO_2 into Formate. *Adv. Energy. Mater.* **12**, 2202695 (2022).
27. Yang, P., Long, Y., Huang, W. & Liu, D. Single-atom copper embedded in two-dimensional MXene toward peroxymonosulfate activation to generate singlet oxygen with nearly 100% selectivity for enhanced Fenton-like reactions. *Appl. Catal. B-Environ. Energy* **324**, (2023).
28. Meng, K., Zhang, J., Zhu, B., Jiang, C., Garcia, H. & Yu, J. Interfacial Charge Transfer in ZnO/COF S-Scheme Photocatalyst via Zn horizontal line N Bond. *Adv. Mater.* **37**, e2505088 (2025).
29. Zhao, Z., et al. Regulating nonradicals generation through peroxymonosulfate activation via localized dipole to enhance wastewater biodegradability. *Nat. Commun.* **16**, 5861 (2025).
30. Yu, X., et al. A green edge-hosted zinc single-site heterogeneous catalyst for superior Fenton-like activity. *Proc. Natl. Acad. Sci. USA.* **120**, e2221228120 (2023).
31. Luo, W., et al. Promoting C-F Bond Activation for Perfluorinated Compounds Decomposition via Atomically Synergistic Lewis and Bronsted Acid Sites. *J. Am. Chem. Soc.* **147**, 7391-7399 (2025).
32. Ye, R., et al. A Ce-CuZn catalyst with abundant Cu/Zn-O_V-Ce active sites for CO_2 hydrogenation to methanol. *Nat. Commun.* **15**, 2159 (2024).
33. Zhang, Z., et al. "Two Ships in a Bottle" Design for Zn-Ag-O Catalyst Enabling Selective and Long-Lasting CO_2 Electroreduction. *J. Am. Chem. Soc.* **143**, 6855-6864 (2021).
34. Chen, Z., An, F., Zhang, Y., Liang, Z., Liu, W. & Xing, M. Single-atom Mo-Co catalyst with low biotoxicity for sustainable degradation of high-ionization-potential organic pollutants. *Proc. Natl.*

Acad. Sci. USA. **120**, e2305933120 (2023).

35. Wang, Z., et al. Cobalt Single Atoms Anchored on Oxygen-Doped Tubular Carbon Nitride for Efficient Peroxymonosulfate Activation: Simultaneous Coordination Structure and Morphology Modulation. *Angew. Chem. Int. Ed.* **61**, 202202338 (2022).
36. Wu, Z., et al. Active Center Size-Dependent Fenton-Like Chemistry for Sustainable Water Decontamination. *Environ. Sci. Technol.* **57**, 21416-21427 (2023).
37. Tian, Q., et al. Silico-oxygen bonding integrated with nano-size pore enrichment enables sustainable low-oxidant-consumption Fenton-like chemistry. *Water Res.* **281**, 123550 (2025).
38. Zhang, D., Li, Y., Wang, P., Qu, J., Li, Y. & Zhan, S. Dynamic active-site induced by host-guest interactions boost the Fenton-like reaction for organic wastewater treatment. *Nat. Commun.* **14**, 3538 (2023).
39. Wang, Z., et al. Non-Radical Activation of Peracetic Acid by Powdered Activated Carbon for the Degradation of Sulfamethoxazole. *Environ. Sci. Technol.* **57**, 10478-10488 (2023).
40. Zhang, Z. Q., et al. Modified-pollen confined hybrid system: A promising union for visible-light-driven photocatalytic antibiotic degradation. *Appl. Catal. B: Environ.* **330**, 122621 (2023).
41. Li, Y. H., et al. Unveiling Roles of Nonradical Electron-Donation Pathway in Peroxymonosulfate Activation for Boosted Interfacial Radical Generation. *Angew. Chem. Int. Ed.* **64**, e202507772 (2025).
42. Zhou, X., et al. Precise Mo-Fe Dual-Atom Coordination Regulates the Selective Generation of Non-Free Radicals in Peroxymoncosulfate Activation. *Adv. Funct. Mater.*, e13232 (2025).
43. Liu, S., et al. How hetero-single-atom dispersion reconstructed electronic structure of carbon materials and regulated Fenton-like oxidation pathways. *Water Res.* **254**, 121417 (2024).
44. Qian, J., Zhang, X., Jia, Y., Xu, H. & Pan, B. Oxidative Polymerization in Water Treatment: Chemical Fundamentals and Future Perspectives. *Environ. Sci. Technol.* **59**, 1060-1079 (2025).
45. Xie, W., et al. Selective polymerization of chlorophenols in hypersaline wastewater via surface-complex-mediated electron transfer over Ce-doped CuO. *Water Res.* **284**, 124023 (2025).

46. Zhu, L., et al. Designing 3D-MoS_2 Sponge as Excellent Cocatalysts in Advanced Oxidation Processes for Pollutant Control. *Angew. Chem. Int. Ed.* **59**, 13968-13976 (2020).
47. Zhang, Z. Q., et al. Photoswitch Mediated Electron Highway Driving Direct Pollutant-to-Oxidant Electron Transfer in Ultrafast Fenton-Like Reactions. *Angew. Chem. Int. Ed.* **65**, e21687 (2026).
48. Zou, W., et al. MoS_2 Nanosheets at Low Doses Induced Cardiotoxicity in Developing Zebrafish via Ferroptosis: Influence of Lateral Size and Surface Modification. *Environ. Sci. Technol.* **58**, 22539-22552 (2024).
49. Wu, C., et al. Mechanisms Underlying the Size-Dependent Neurotoxicity of Polystyrene Nanoplastics in Zebrafish. *Environ. Sci. Technol.* **59**, 1577-1586 (2025).
50. Wang, C., Yang, X., Zheng, Q., Moe, B. & Li, X. F. Halobenzoquinone-Induced Developmental Toxicity, Oxidative Stress, and Apoptosis in Zebrafish Embryos. *Environ. Sci. Technol.* **52**, 10590-10598 (2018).
51. Ranasinghe, T., Seo, Y., Park, H. C., Choe, S. K. & Cha, S. H. Rotenone exposure causes features of Parkinson;s disease pathology linked with muscle atrophy in developing zebrafish embryo. *J. Hazard. Mater.* **480**, 136215 (2024).
52. Feng, Y., et al. Effect of microcystin-LR on intestinal microbiota, metabolism, and health of zebrafish (Danio rerio). *Sci. Total. Environ.* **967**, 178838 (2025).
53. Li, J., et al. Spatial multi-omics analysis of metabolic heterogeneity in zebrafish exposed to microcystin-LR and its disinfection byproducts. *Water Res.* **280**, 123599 (2025).
54. Yu, H., et al. Developmental hepatotoxicity and lipid metabolic disruption induced by fluxapyroxad in zebrafish embryos: An integrative omics approach. *Ecotox. Environ. Safe.* **303**, 119035 (2025).
55. Zhu, B., et al. Impact of 1,2-Bis (2,4,6-Tribromophenoxy) Ethane on Liver Metabolism and Intestinal Health in Zebrafish: Role of the Liver X Receptor. *Environ. Sci. Technol.* **59**, 8439-8450 (2025).
56. Wei, S., et al. The guanine nucleotide exchange factor Net1 facilitates the specification of dorsal

cell fates in zebrafish embryos by promoting maternal beta-catenin activation. *Cell Res.* **27**, 202-225 (2017).

57. Li, N., et al. Dual-functional DNA nanoribbon-templated copper nanoclusters synergistically activate NRF2/HO-1 pathway for synergistic oxidative stress mitigation. *J. Colloid. Interface. Sci.* **702**, 138837 (2025).
58. Jiang, N., et al. Evaluation of the biological response of propofol in zebrafish (Danio rerio): Focusing on biochemical, transcriptional, and molecular level. *Environ. Pollut.* **317**, 120764 (2023).

Acknowledgments

The authors thank the National Natural Science Foundation of China (225B2602, 52270149), New Chongqing Youth Innovative Talent Program (CSTB2025YITP-QCRCX0056), and the Fundamental Research Funds for the Central Universities grant (2024IAIS-QN013) for supporting this work. The authors also thank Scientific Compass (www.shiyanjia. com) for supporting the related characterizations.

Author contributions

F. Chen and Z. Q. Zhang conceived and planned the experiments. Z. Q. Zhang performed the relevant experiments. P. J. Duan performed the theoretical calculations. Y. Shao supervised the zebrafish experiments. Z.Q. Zhang, X.W. Xu, P. J. Duan, Z. H. Qin, Q. Wang, Y. Shao, C. W. Bai, X. J. Chen, J. Wang, F. Q. Yang, and F. Chen assisted in analyzing various characterizations. Z. Q. Zhang wrote the initial draft, X.W. Xu, P. J. Duan and F. Chen further modified the manuscript.

Competing interests

The authors declare no competing interests.

Data availability

The data supporting the findings of the study are included in the main text and supplementary information files. Raw data can be obtained from the corresponding authors upon request. Source data are provided in this paper.

Figure Captions

Fig. 1. | Design principles and research approach for dual-substrate systems activated by dual-function site catalysts. a, Comparative advantages of polymerization and mineralization processes. **b,** Design concept for dual-substrate activation over bifunctional site catalysts. **c**, Transition in the mechanism of bifunctional site catalysts during the activation of pollutants with different electronic types and the potential synergistic and complementary processes between them.

Fig. 2. | Validation of ZnO/CuO heterostructures with dual Zn and Cu sites. a, Schematic of ZnO/CuO synthesis. **b,** XRD patterns of ZnO, CuO, and ZnO/CuO. **c**, FTIR spectra of ZnO, CuO, and ZnO/CuO. **d,** TEM image of ZnO/CuO. **e,** High-resolution TEM (HRTEM) image of ZnO in ZnO/CuO (inset: lattice fringes of ZnO; edge smoothing was applied with a filter setting of 20 pixels to enhance the image clarity; *d*=0.245nm, FFT image derived from Supplementary Fig. 5a). **f,** HRTEM image of CuO in ZnO/CuO (inset: lattice fringes of CuO; edge smoothing was applied with a filter setting of 20 pixels to enhance the image clarity; *d*=0.253nm, FFT image derived from Supplementary Fig. 6a). Data are representative of two independent experiments, both yielding similar results. **g**, Zn 2*p* XPS spectra of ZnO and ZnO/CuO. **h**, Cu 2*p* XPS spectra of CuO and ZnO/CuO. **i,** Normalized Zn *K*-edge XANES spectra of ZnO/CuO sample with Zn foil and ZnO standards (inset: magnified region). **j,** Normalized Cu *K*-edge XANES spectra of ZnO/CuO sample with Cu foil, Cu_2O, and CuO standards (inset: magnified region). **k,** k_3-weighted FT-EXAFS spectra of ZnO/CuO with Zn foil and ZnO references. **l,** k_3-weighted FT -EXAFS spectra of ZnO/CuO with Cu foil, Cu_2O, and CuO references. **m,** WT-EXAFS (Zn *K*-edge) of ZnO/CuO. **n,** WT-EXAFS (Cu *K*-edge) of ZnO/CuO.

Fig. 3. | Removal performance and environmental robustness of the constructed Fenton-like system. a, BPA degradation in different reaction systems (Conditions: $[\text{Catal.}]_0 = 0.2\ \text{g L}^{-1}$, $[\text{PMS}]_0 = 0.3$ mM, $[\text{pH}]_0 = 6.96$, $[\text{BPA}]_0 = 10\ \text{mg L}^{-1}$, [Temp.]= 20±2 °C). **b,** Comparison of BPA removal efficiencies and apparent rate constants across systems. **c,** Reported modified rate constants (*k*-value) for BPA and ATZ removal versus this work (Detailed information is available in Supplementary Table 18). **d,** ATZ degradation

in different reaction systems (Conditions: $[\mathrm{Catal.}]_0 = 0.2$ g L^{-1}, $[\mathrm{PMS}]_0 = 0.5$ mM, $[\mathrm{pH}]_0 = 7.03$, $[\mathrm{ATZ}]_0 = 10$ mg L^{-1}, [Temp.]= 20±2 °C). **e,** Comparison of ATZ degradation efficiencies and apparent rate constants. **f,** Effect of dissolved organic matter surrogates (humic acid, HA; bovine serum albumin, BSA) on BPA and ATZ degradation. **g**, BPA and ATZ degradation by ZnO/CuO/PMS system at different initial pH values. **h**, Substrate scope: degradation of representative pollutants by ZnO/CuO/PMS system. The error bars in **b, e, f** represent the standard deviation of three replicate tests. **i,** Adsorption configurations of dual substrates on bifunctional sites. **j,** Catalyst deactivation during polymerization and its regeneration via in situ radical-driven depolymerization in the mineralization process.

Fig. 4. | Active-species identification and electrochemical diagnostics. **a,** BPA degradation in the ZnO/CuO/PMS system with quenchers ([TBA] = [MeOH] = 50 mM, [TEMPOL] = [p-BQ]= 1 mM, [*L*-histidine] = [*β*-carotene] =1 mM, [PMSO] = 1 mM, [DMSO] = 20 mM). **b**, BPA degradation by the ZnO/CuO/PMS reaction system in the presence of different TBA and MeOH concentrations. **c,** ATZ degradation by the ZnO/CuO/PMS reaction system in the presence of different TBA and MeOH concentrations. The error bars in **a-c** represent the standard deviation of three replicate tests. **d,** DMPO spin-trapping ESR spectra for DMPO-$SO_4^{\bullet-}$ and TEMP-based ESR spectra for $^1O_2$ in the ZnO/CuO/PMS/BPA system. **e,** DMPO spin-trapping ESR spectra for DMPO-$SO_4^{\bullet-}$ in the ZnO/CuO/PMS/ATZ system. **f,** Open-circuit potentials (OCP) changes upon sequential addition of PMS and contaminants (inset: *i-t* (current-time) curves). **g,** Electrochemical impedance spectra (EIS) of catalysts (inset: EIS for ZnO/CuO under different conditions). **h,** Linear sweep voltammetry (LSV) of catalyst electrodes (inset: LSV curves of ZnO/CuO electrodes under different conditions).

Fig. 5. | Dual-site functions and reaction pathway analysis. **a**, *In-situ* Raman spectra in different ZnO/CuO systems. **b**, *In-situ* Raman spectra in different CuO systems. **c**, *In-situ* Raman spectra in different ZnO systems. **d**, Comparison of adsorption energies for PMS on Zn and Cu Sites in ZnO/CuO catalysts. **e**, Comparison of adsorption energies for BPA and ATZ on ZnO and ZnO/CuO catalysts. **f**, Comparison of adsorption energies for BPA and ATZ on CuO and ZnO/CuO catalysts. **g,** pDOS of ZnO, CuO, and ZnO/CuO

(pDOS: projected density of states). **h**, Calculated work functions of ZnO and CuO. **i**, Schematic of built-in electric field and interfacial charge transfer in ZnO/CuO. **j**, Energy gap difference between the LUMO of the ZnO/PMS complex and the HOMO of each pollutant.

Fig. 6. | In-Situ depolymerization and pilot-scale validation. **a**, Simultaneous removal of BPA and ATZ by ZnO/CuO/PMS. The error bars in **a** represent the standard deviation of three replicate tests. **b,** TGA curves of ZnO/CuO before and after reaction with BPA (inset: TGA curves recorded upon treatment of the post-reaction catalyst with PMS/H_2O versus PMS/ATZ). **c**, Surface C and O atomic contents for pristine ZnO/CuO, after BPA/PMS, and after ATZ/PMS depolymerization. **d,** BPA removal by polymer-fouled ZnO/CuO versus the same catalyst after ATZ/PMS depolymerization. **e,** BPA recycling performance with and without ATZ ($[BPA]_0 = 10$ mg L^{-1}, $[ATZ]_0 = 2$ mg L^{-1}). **f,** TEM images of ZnO/CuO after polymerization and after depolymerization. Data are representative of two independent experiments, both yielding similar results. **g,** Schematic diagram of a water-driven self-circulating reactor. **h,** Photograph of sponge-supported catalyst in the reactor. **i,** Ten-cycle treatment of 200 L mixed wastewater (BPA + ATZ) by ZnO/CuO/PMS.

Fig. 7. | Comprehensive toxicity assessment under realistic conditions. **a,** Zebrafish survival and deformity ratios across treatment systems. **b,** Heartbeat counts (per 20 seconds) of zebrafish at 48-96 h post-fertilization (hpf: hours post fertilization). The error bars in **b** represent the standard deviation of five replicate tests. **c,** Zebrafish body length comparisons (the curve is a normal distribution curve). **d**, Representative image of zebrafish in blank solution. **e**, Zebrafish in ZnO/CuO/PMS/BPA-treated solution. **f**, Zebrafish in ZnO/CuO/PMS/ATZ-treated solution (scale bar, 1 mm). Representative images of intracellular ROS production detected by fluorescent staining in zebrafish at 120 hpf: (**g**) blank group, (**h**) BPA-treated group, and (**i**) BPA-untreated group. Data are representative of two independent experiments, both yielding similar results. **j**, Volcano plot of differentially expressed genes between the BPA-treated group and the untreated group. Statistical analysis: two-tailed t-test with Benjamini-Hochberg (BH) correction ($P = 0.05$). **k**, Marker metabolites differing between the two groups. **l**, Top 20 enriched KEGG pathways for BPA-treated *vs.* untreated groups (Rich factor: ratio of differentially abundant metabolites to total metabolites annotated in a

given pathway). Statistical analysis: one-tailed hypergeometric test with BH correction.

Editorial Summary

A ZnO/CuO catalyst featuring dual-site cooperative framework for polymerization-based wastewater treatment. Zn sites preferentially adsorb/activate organics, whereas Cu sites predominantly activate the oxidant, showcasing atomic-scale design to reactor-scale implementation.

Peer review information: *Nature Communications* thanks Hongjun Liu, and the other, anonymous, reviewer(s) for their contribution to the peer review of this work. A peer review file is available.

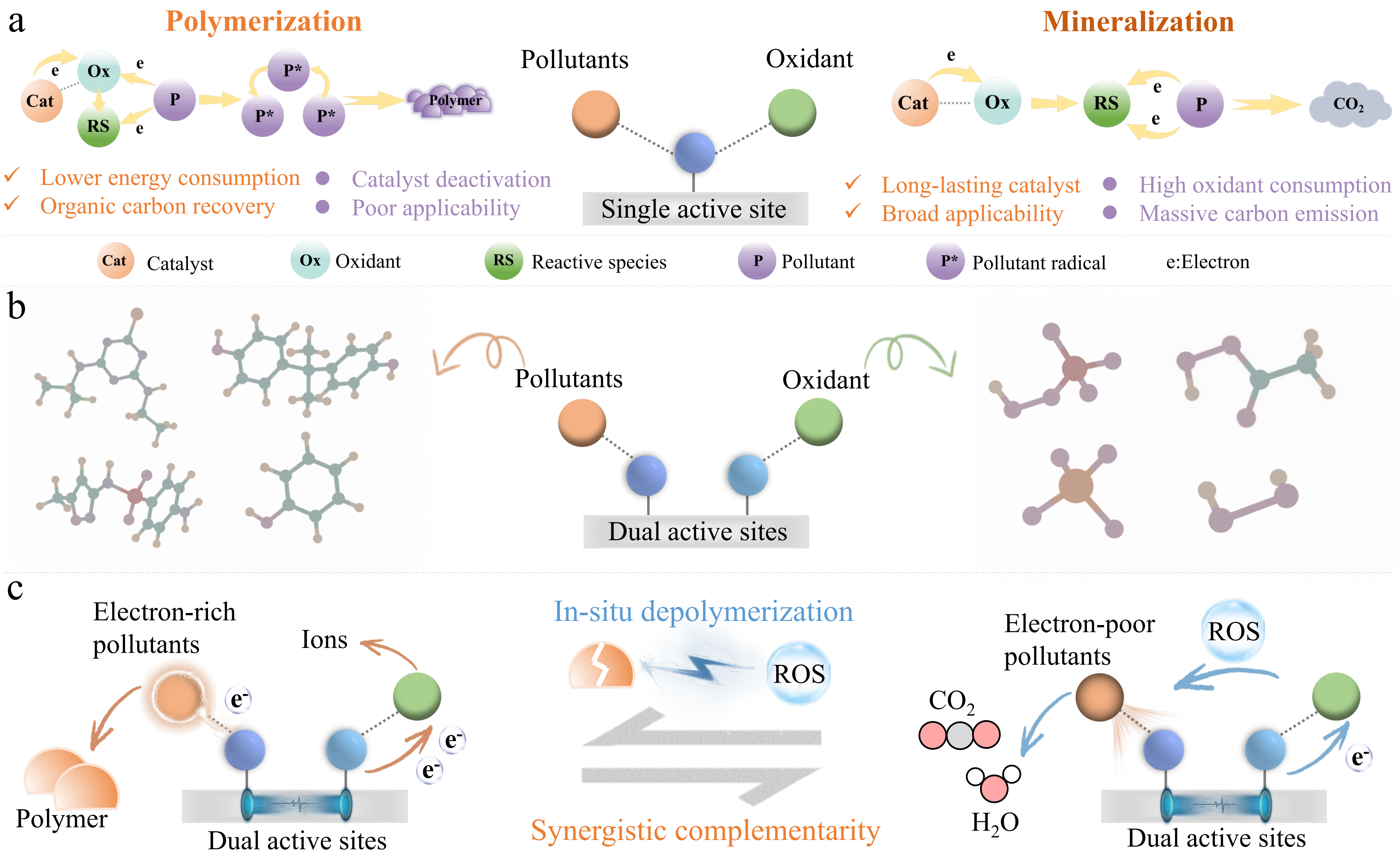
a
Polymerization
e
Ox
e
Cat
P
P*
P*
P*
Polymer
RS
e
✓ Lower energy consumption
✓ Organic carbon recovery
● Catalyst deactivation
● Poor applicability
Pollutants
Oxidant
Single active site
Mineralization
e
Cat
Ox
RS
e
e
P
CO_2
✓ Long-lasting catalyst
✓ Broad applicability
● High oxidant consumption
● Massive carbon emission
Cat Catalyst
Ox Oxidant
RS Reactive species
P Pollutant
P* Pollutant radical
e:Electron
b
Pollutants
Oxidant
Dual active sites
c
Electron-rich pollutants
Ions
e^-
e^-
e^-
Polymer
Dual active sites
In-situ depolymerization
ROS
Synergistic complementarity
Electron-poor pollutants
ROS
CO_2
H_2O
e^-
Dual active sites

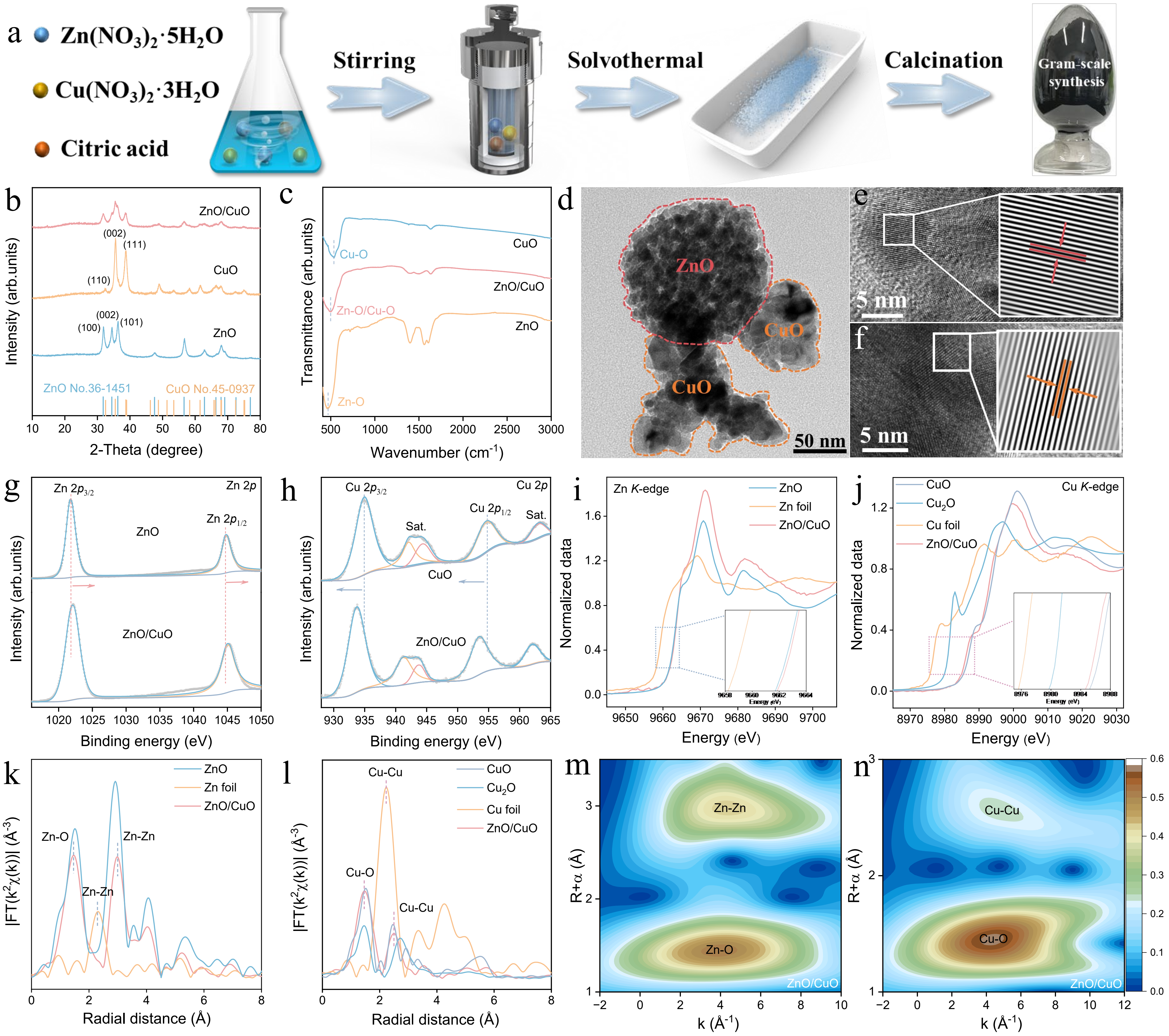
a
$Zn(NO_3)_2·5H_2O$
$Cu(NO_3)_2·3H_2O$
Citric acid
Stirring
Solvothermal
Calcination
Gram-scale synthesis
b
ZnO/CuO
CuO
ZnO
(002)
(111)
(110)
(100)
(101)
ZnO No.36-1451
CuO No.45-0937
Intensity (arb.units)
2-Theta (degree)
c
Cu-O
Zn-O/Cu-O
Zn-O
CuO
ZnO/CuO
ZnO
Transmittance (arb.units)
Wavenumber (cm^{-1})
d
ZnO
CuO
CuO
50 nm
e
5 nm
f
5 nm
g
Zn $2p_{3/2}$
Zn 2p
Zn $2p_{1/2}$
ZnO
ZnO/CuO
Intensity (arb.units)
Binding energy (eV)
h
Cu $2p_{3/2}$
Cu 2p
Cu $2p_{1/2}$
Sat.
Sat.
CuO
ZnO/CuO
Intensity (arb.units)
Binding energy (eV)
i
Zn K-edge
ZnO
Zn foil
ZnO/CuO
Normalized data
Energy (eV)
j
CuO
Cu_2O
Cu foil
ZnO/CuO
Cu K-edge
Normalized data
Energy (eV)
k
ZnO
Zn foil
ZnO/CuO
Zn-O
Zn-Zn
Zn-Zn
$|FT(k^2\chi(k))|$ (Å^{-3})
Radial distance (Å)
l
CuO
Cu_2O
Cu foil
ZnO/CuO
Cu-Cu
Cu-O
Cu-Cu
$|FT(k^2\chi(k))|$ (Å^{-3})
Radial distance (Å)
m
Zn-Zn
Zn-O
ZnO/CuO
R+α (Å)
k (Å^{-1})
n
Cu-Cu
Cu-O
ZnO/CuO
R+α (Å)
k (Å^{-1})

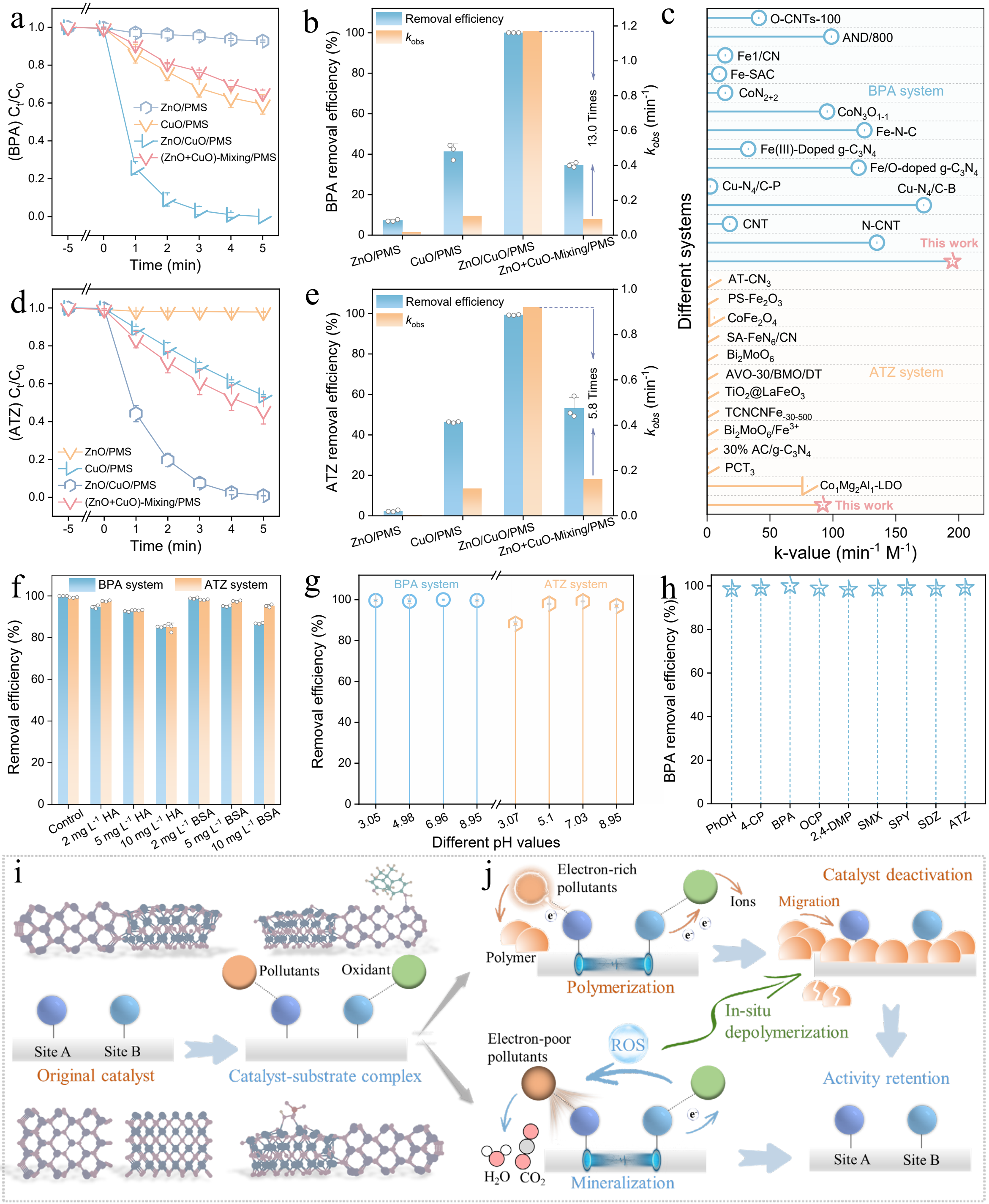
a
(BPA) C_t/C_0
Time (min)
ZnO/PMS
CuO/PMS
ZnO/CuO/PMS
(ZnO+CuO)-Mixing/PMS
b
BPA removal efficiency (%)
Removal efficiency
k_{obs}
k_{obs} (min^{-1})
13.0 Times
ZnO/PMS
CuO/PMS
ZnO/CuO/PMS
ZnO+CuO-Mixing/PMS
c
Different systems
O-CNTs-100
AND/800
Fe1/CN
Fe-SAC
CoN$_{2+2}$
BPA system
CoN$_3$O$_{1-1}$
Fe-N-C
Fe(III)-Doped g-C$_3$N$_4$
Fe/O-doped g-C$_3$N$_4$
Cu-N$_4$/C-P
Cu-N$_4$/C-B
CNT
N-CNT
This work
AT-CN$_3$
PS-Fe$_2$O$_3$
CoFe$_2$O$_4$
SA-FeN$_6$/CN
Bi$_2$MoO$_6$
AVO-30/BMO/DT
ATZ system
TiO$_2$@LaFeO$_3$
TCNCNFe$_{30\text{-}500}$
Bi$_2$MoO$_6$/Fe^{3+}
30% AC/g-C$_3$N$_4$
PCT$_3$
Co$_1$Mg$_2$Al$_1$-LDO
This work
k-value (min^{-1} M^{-1})
d
(ATZ) C_t/C_0
Time (min)
ZnO/PMS
CuO/PMS
ZnO/CuO/PMS
(ZnO+CuO)-Mixing/PMS
e
ATZ removal efficiency (%)
Removal efficiency
k_{obs}
k_{obs} (min^{-1})
5.8 Times
ZnO/PMS
CuO/PMS
ZnO/CuO/PMS
ZnO+CuO-Mixing/PMS
f
Removal efficiency (%)
BPA system
ATZ system
Control
2 mg L^{-1} HA
5 mg L^{-1} HA
10 mg L^{-1} HA
2 mg L^{-1} BSA
5 mg L^{-1} BSA
10 mg L^{-1} BSA
g
Removal efficiency (%)
BPA system
ATZ system
3.05
4.98
6.96
8.95
3.07
5.1
7.03
8.95
Different pH values
h
BPA removal efficiency (%)
PhOH
4-CP
BPA
OCP
2,4-DMP
SMX
SPY
SDZ
ATZ
i
Pollutants
Oxidant
Site A
Site B
Original catalyst
Catalyst-substrate complex
j
Electron-rich pollutants
Ions
Polymer
Polymerization
Catalyst deactivation
Migration
In-situ depolymerization
Electron-poor pollutants
ROS
H$_2$O
CO$_2$
Mineralization
Activity retention
Site A
Site B

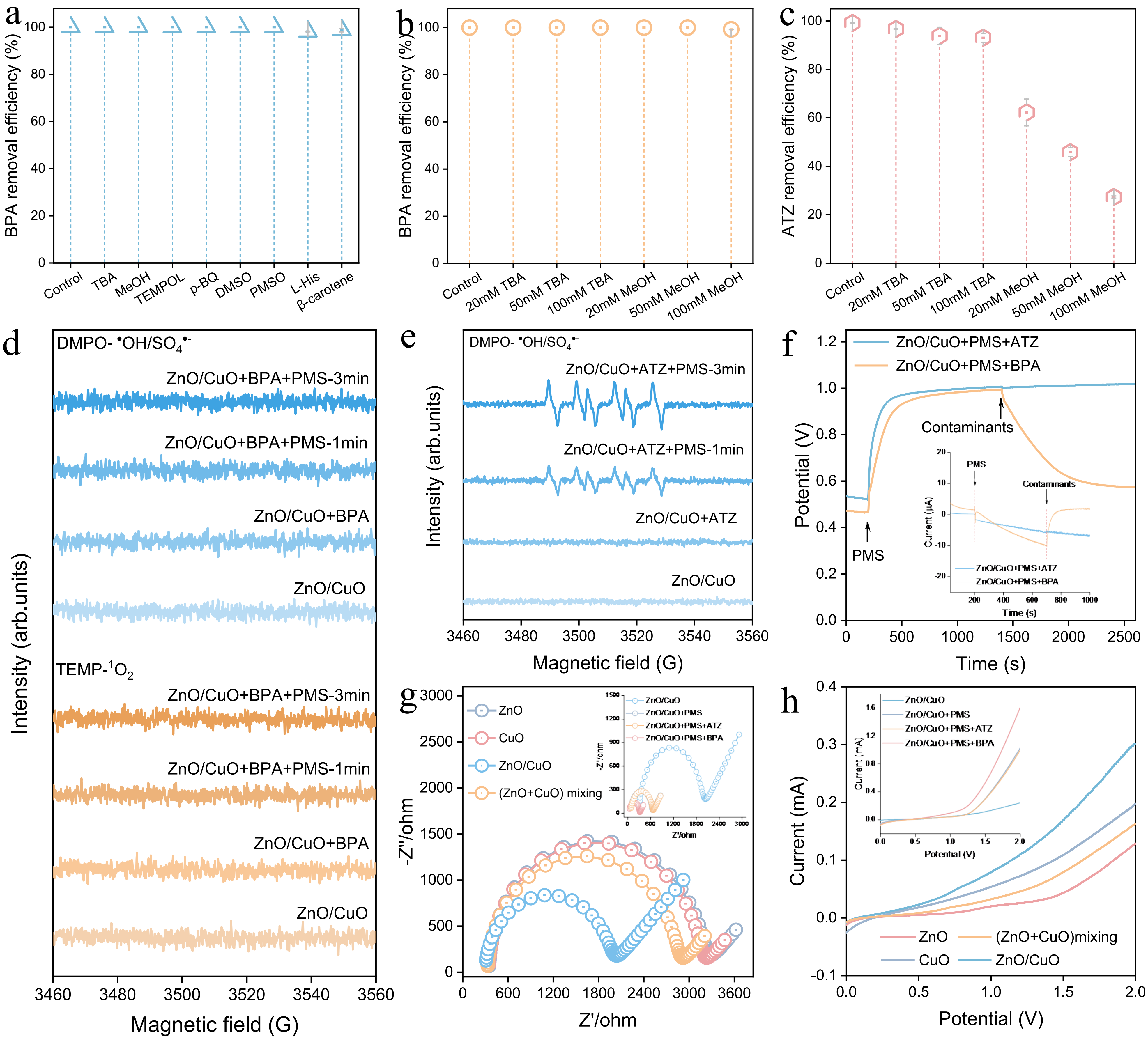
a
BPA removal efficiency (%)
Control
TBA
MeOH
TEMPOL
p-BQ
DMSO
PMSO
L-His
β-carotene
b
BPA removal efficiency (%)
Control
20mM TBA
50mM TBA
100mM TBA
20mM MeOH
50mM MeOH
100mM MeOH
c
ATZ removal efficiency (%)
Control
20mM TBA
50mM TBA
100mM TBA
20mM MeOH
50mM MeOH
100mM MeOH
d
DMPO- •OH/SO$_4$•-
ZnO/CuO+BPA+PMS-3min
ZnO/CuO+BPA+PMS-1min
ZnO/CuO+BPA
ZnO/CuO
TEMP-^{1}O$_2$
ZnO/CuO+BPA+PMS-3min
ZnO/CuO+BPA+PMS-1min
ZnO/CuO+BPA
ZnO/CuO
Intensity (arb.units)
Magnetic field (G)
e
DMPO- •OH/SO$_4$•-
ZnO/CuO+ATZ+PMS-3min
ZnO/CuO+ATZ+PMS-1min
ZnO/CuO+ATZ
ZnO/CuO
Intensity (arb.units)
Magnetic field (G)
f
ZnO/CuO+PMS+ATZ
ZnO/CuO+PMS+BPA
Contaminants
PMS
Potential (V)
Time (s)
Current (μA)
Time (s)
g
ZnO
CuO
ZnO/CuO
(ZnO+CuO) mixing
ZnO/CuO
ZnO/CuO+PMS
ZnO/CuO+PMS+ATZ
ZnO/CuO+PMS+BPA
-Z''/ohm
Z'/ohm
h
ZnO/CuO
ZnO/CuO+PMS
ZnO/CuO+PMS+ATZ
ZnO/CuO+PMS+BPA
Current (mA)
Potential (V)
ZnO
(ZnO+CuO)mixing
CuO
ZnO/CuO
Current (mA)
Potential (V)

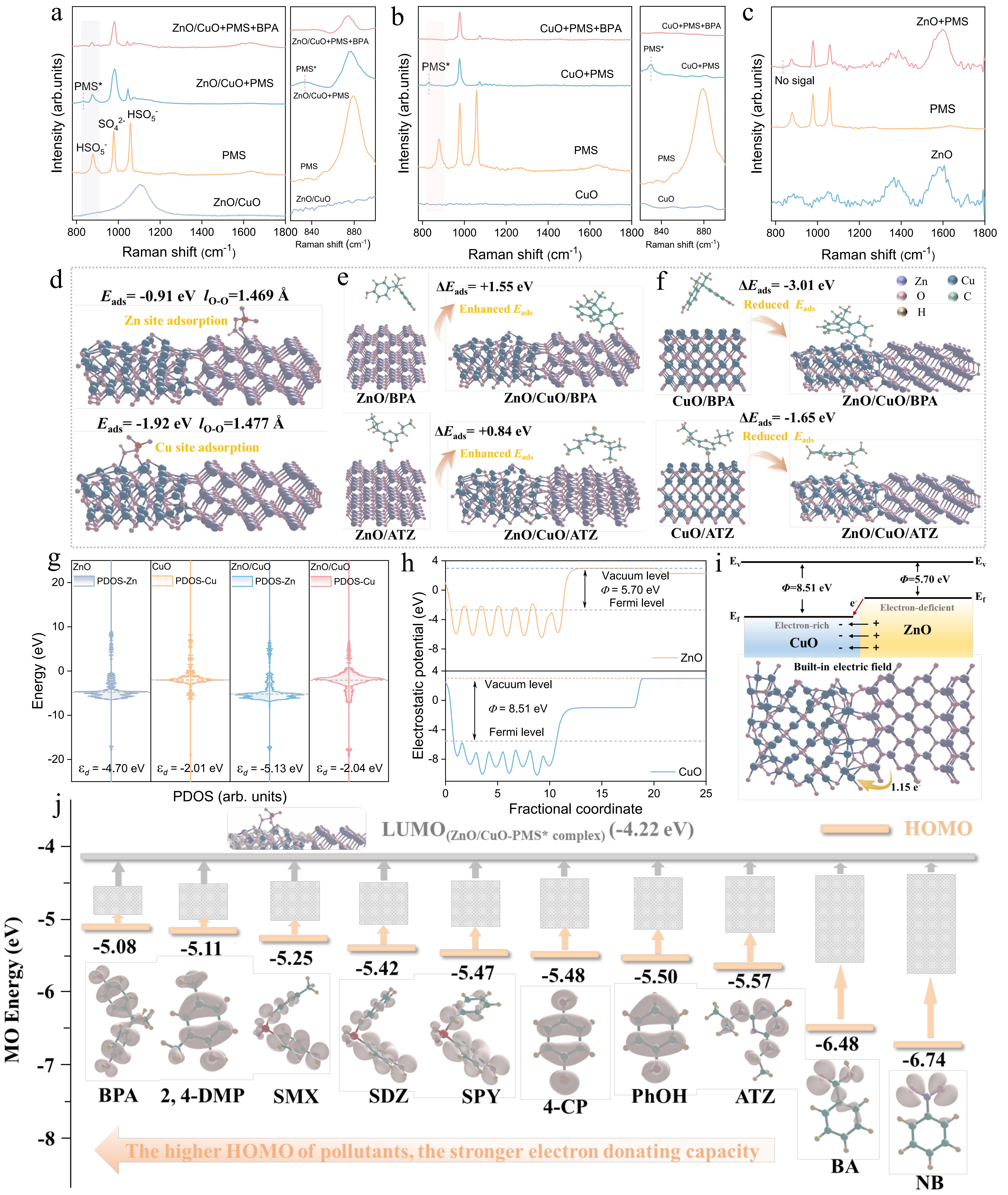
a
ZnO/CuO+PMS+BPA
ZnO/CuO+PMS
PMS*
SO_4^{2-}
HSO_5^-
HSO_5^-
PMS
ZnO/CuO
Intensity (arb.units)
Raman shift (cm^{-1})
800 1000 1200 1400 1600 1800
840 880
b
CuO+PMS+BPA
CuO+PMS
PMS*
PMS
CuO
c
ZnO+PMS
No sigal
PMS
ZnO
d
E_{ads}= -0.91 eV l_{O-O}=1.469 Å
Zn site adsorption
E_{ads}= -1.92 eV l_{O-O}=1.477 Å
Cu site adsorption
e
ΔE_{ads}= +1.55 eV
Enhanced E_{ads}
ZnO/BPA
ZnO/CuO/BPA
ΔE_{ads}= +0.84 eV
Enhanced E_{ads}
ZnO/ATZ
ZnO/CuO/ATZ
f
ΔE_{ads}= -3.01 eV
Reduced E_{ads}
CuO/BPA
ZnO/CuO/BPA
ΔE_{ads}= -1.65 eV
Reduced E_{ads}
CuO/ATZ
ZnO/CuO/ATZ
Zn Cu O C H
g
ZnO PDOS-Zn
CuO PDOS-Cu
ZnO/CuO PDOS-Zn
ZnO/CuO PDOS-Cu
Energy (eV)
PDOS (arb. units)
ε_d = -4.70 eV
ε_d = -2.01 eV
ε_d = -5.13 eV
ε_d = -2.04 eV
h
Vacuum level
Φ = 5.70 eV
Fermi level
ZnO
Vacuum level
Φ = 8.51 eV
Fermi level
CuO
Electrostatic potential (eV)
Fractional coordinate
i
E_v
Φ=8.51 eV
Φ=5.70 eV
E_f
Electron-rich
CuO
Electron-deficient
ZnO
Built-in electric field
1.15 e$^-$
j
LUMO$_{(ZnO/CuO-PMS^*\ complex)}$ (-4.22 eV)
HOMO
MO Energy (eV)
-5.08 -5.11 -5.25 -5.42 -5.47 -5.48 -5.50 -5.57 -6.48 -6.74
BPA 2, 4-DMP SMX SDZ SPY 4-CP PhOH ATZ BA NB
The higher HOMO of pollutants, the stronger electron donating capacity

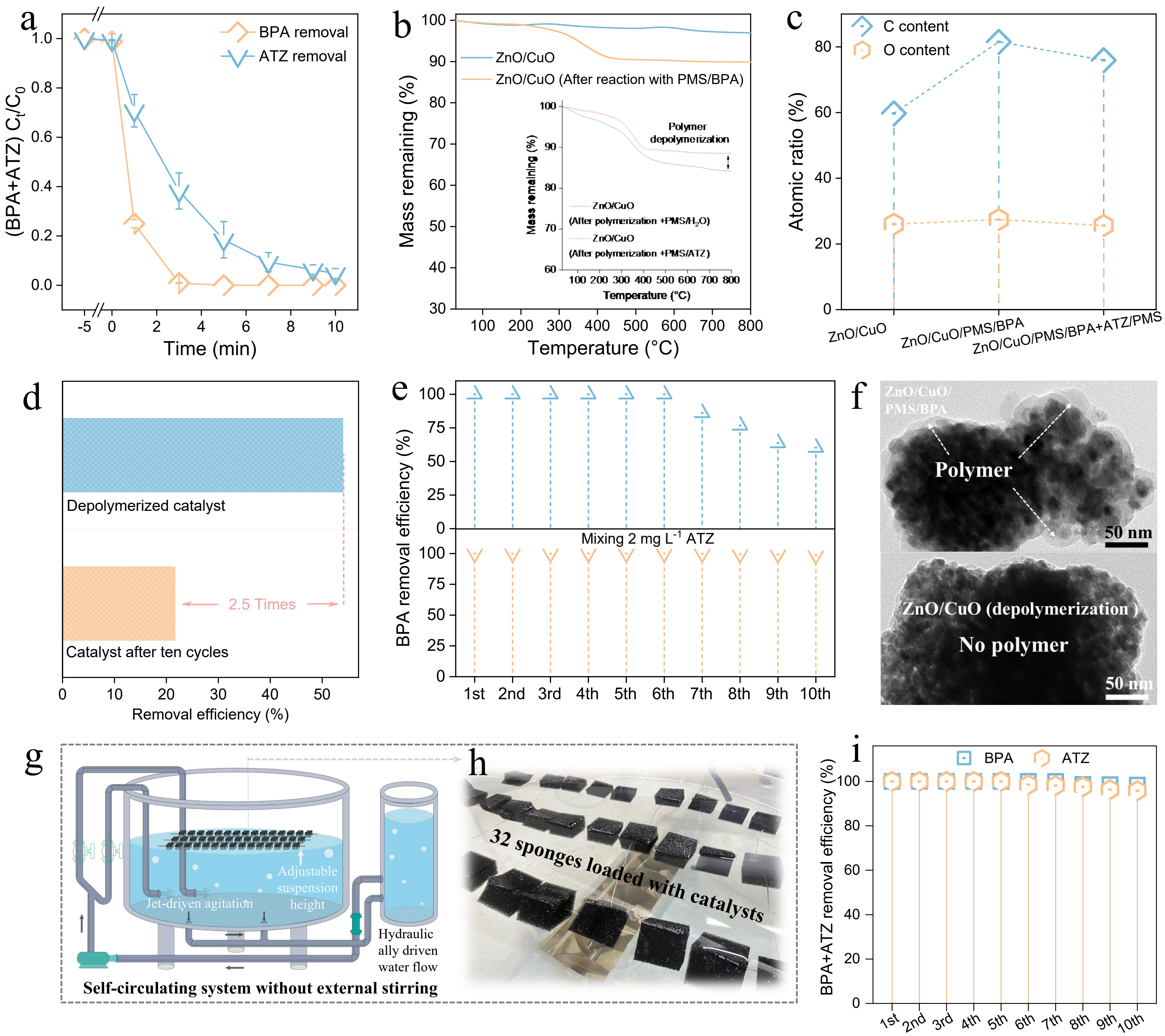
a
BPA removal
ATZ removal
(BPA+ATZ) C$_t$/C$_0$
1.0
0.8
0.6
0.4
0.2
0.0
-5
0
2
4
6
8
10
Time (min)
b
ZnO/CuO
ZnO/CuO (After reaction with PMS/BPA)
Mass remaining (%)
100
90
80
70
60
50
40
30
100
200
300
400
500
600
700
800
Temperature (°C)
Polymer depolymerization
ZnO/CuO (After polymerization +PMS/H$_2$O)
ZnO/CuO (After polymerization +PMS/ATZ)
Mass remaining (%)
Temperature (°C)
c
C content
O content
Atomic ratio (%)
80
60
40
20
0
ZnO/CuO
ZnO/CuO/PMS/BPA
ZnO/CuO/PMS/BPA+ATZ/PMS
d
Depolymerized catalyst
2.5 Times
Catalyst after ten cycles
0
10
20
30
40
50
Removal efficiency (%)
e
BPA removal efficiency (%)
100
75
50
25
0
Mixing 2 mg L^{-1} ATZ
1st
2nd
3rd
4th
5th
6th
7th
8th
9th
10th
f
ZnO/CuO/PMS/BPA
Polymer
50 nm
ZnO/CuO (depolymerization)
No polymer
50 nm
g
Adjustable suspension height
Jet-driven agitation
Hydraulically driven water flow
Self-circulating system without external stirring
h
32 sponges loaded with catalysts
i
BPA
ATZ
BPA+ATZ removal efficiency (%)
100
80
60
40
20
0
1st
2nd
3rd
4th
5th
6th
7th
8th
9th
10th

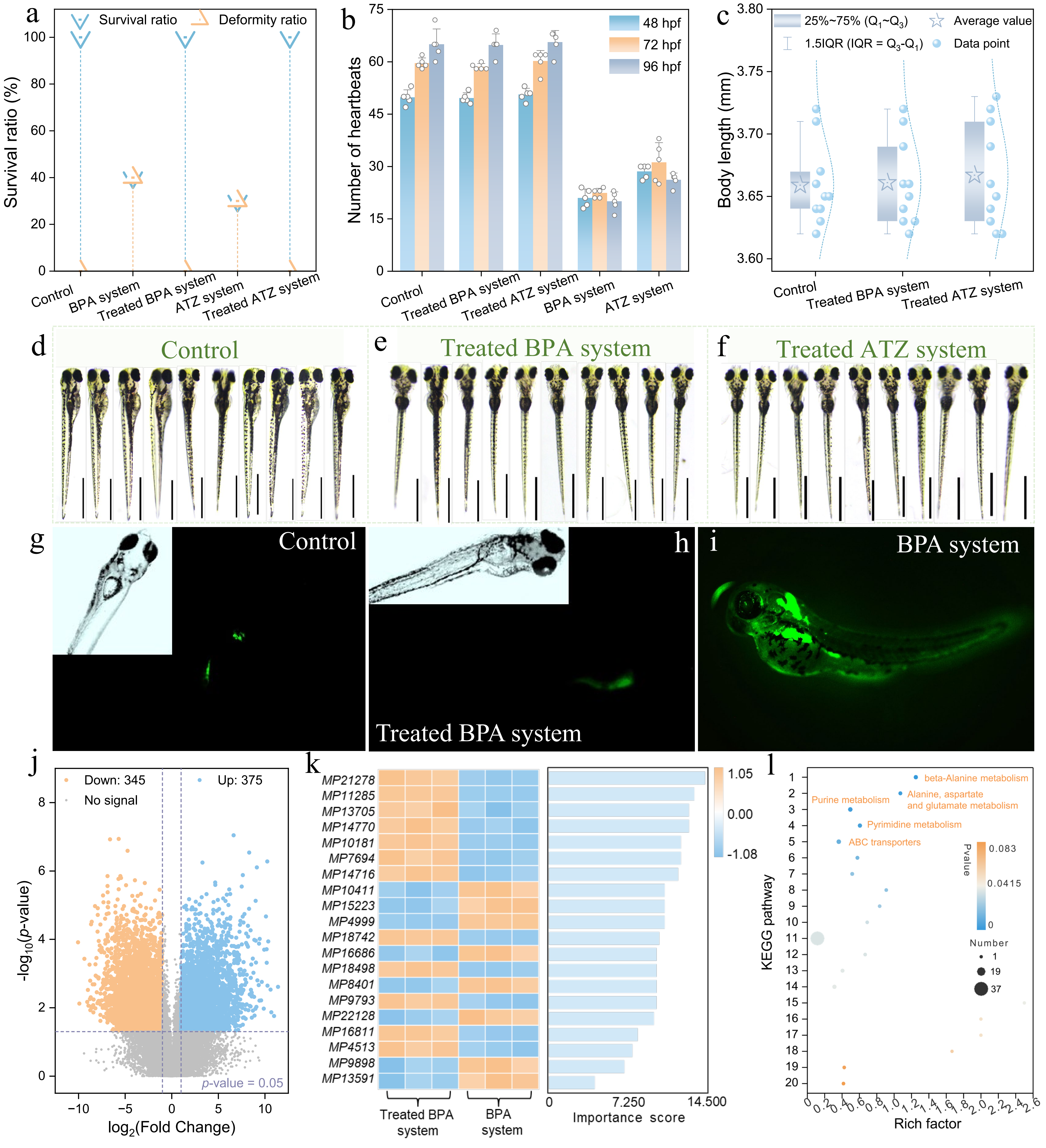
a
Survival ratio
Deformity ratio
Survival ratio (%)
0
20
40
60
80
100
Control
BPA system
Treated BPA system
ATZ system
Treated ATZ system
b
Number of heartbeats
0
15
30
45
60
75
48 hpf
72 hpf
96 hpf
Control
Treated BPA system
Treated ATZ system
BPA system
ATZ system
c
Body length (mm)
3.60
3.65
3.70
3.75
3.80
25%~75% (Q1~Q3)
Average value
1.5IQR (IQR = Q3-Q1)
Data point
Control
Treated BPA system
Treated ATZ system
d
Control
e
Treated BPA system
f
Treated ATZ system
g
Control
h
Treated BPA system
i
BPA system
j
Down: 345
Up: 375
No signal
-log10(p-value)
log2(Fold Change)
p-value = 0.05
-10
-5
0
5
10
0
2
4
6
8
k
MP21278
MP11285
MP13705
MP14770
MP10181
MP7694
MP14716
MP10411
MP15223
MP4999
MP18742
MP16686
MP18498
MP8401
MP9793
MP22128
MP16811
MP4513
MP9898
MP13591
Treated BPA system
BPA system
1.05
0.00
-1.08
0
7.250
14.500
Importance score
l
KEGG pathway
Rich factor
beta-Alanine metabolism
Purine metabolism
Alanine, aspartate and glutamate metabolism
Pyrimidine metabolism
ABC transporters
Pvalue
0.083
0.0415
0
Number
1
19
37
1
2
3
4
5
6
7
8
9
10
11
12
13
14
15
16
17
18
19
20
0
0.2
0.4
0.6
0.8
1.0
1.2
1.4
1.6
1.8
2.0
2.2
2.4
2.6